Corrosion Science 153 (2019) 341–356

Contents lists available at ScienceDirect

Corrosion Science

journal homepage: www.elsevier.com/locate/corsci

Influences of albumin on *in vitro* corrosion of pure Zn in artificial plasma

Lijun Liu[a], Yao Meng[a], Alex A. Volinsky[b], Hai-Jun Zhang[c], Lu-Ning Wang[a,*]

[a] Beijing Advanced Innovation Centre for Materials Genome Engineering, School of Materials Science and Engineering, University of Science and Technology Beijing, Beijing, 100083, China

[b] Department of Mechanical Engineering, University of South Florida, Tampa, FL, 33620, USA

[c] National United Engineering Laboratory for Biomedical Material Modification, Qihe, Shandong Province, 251100, China

ARTICLE INFO

Keywords:
Zinc
Stent
Corrosion
Artificial plasma
Albumin

ABSTRACT

Influences of albumin on in vitro corrosion behaviour of pure Zn in artificial plasma up to 28 days were investigated. Pure Zn undergoes uniform corrosion and a complex of albumin and zinc oxide/hydroxide forms on the surface. At the initial immersion stage, rapid adsorption of albumin retards the corrosion of pure Zn. However, the corrosion is promoted due to dissolution of metal matrix after 3 days. And 7 days later, Zn corrosion is obstructed by the complex accumulation on the surfaces. Profound understanding of pure Zn corrosion will encourage further exploration of Zn alloys in potential clinical application.

1. Introduction

Recently, there have been an up-surge interest in the potential use of zinc (Zn) and its alloys as coronary artery stents due to their unique advantages, ideal degradation rate in vivo, over conventional biodegradable metallic materials. This is mainly attributed to their favourable biological merits and biodegradability [1–6]. Zn degrades naturally under physiological environment. It possesses standard electrochemical potential between that of magnesium and iron, implying an appropriate physiological degradation rate [7]. Thus it is considered as potential candidate for biodegradable coronary stents. Practically, it was found that Zn proceeds of a degradation rate of ~20 μm y^{-1} in rat arteries, which appears to be ideal for stent application [8]. The biocompatibility of a material is another concern in the development of biodegradable materials. Zn is considered to be an essential trace element and to take part in many important biological reactions [9–12]. Some in vivo tests revealed that Zn exhibited a strong antiatherogenic character [13], good hemocompatibility [14] along with non-cytotoxicity to endothelial cell [15].

Corrosion behaviour, including corrosion rate and evolution of corrosion products, is crucial for understanding the basic corrosion processes underpinning absorption of biodegradable metals. As stent materials, Zn-based alloys are supposed to contact with the human blood after implantation. To date, numerous efforts have been devoted to addressing the in vitro corrosion behaviour of Zn-based material in simulated physiological conditions [16–19]. Nevertheless, no consensus has been reached for the corrosion mechanism of pure Zn. Cheng et al [16] concluded that the corrosion rate of pure Zn was between Fe and Mn in Hank's solution. Chen et al [17] found that the corrosion rate placed Zn between Fe and Mg in phosphate buffered saline (PBS) in transient assays. However, in contrary to Cheng's study, in a long-term course the corrosion rate of Zn developed faster than that of Fe and Mg. To better understand its corrosion behaviour, Törne et al [20] compared the degradation of pure Zn in saline solutions, plasma and whole blood up to 72 h. They suggested that passivation films containing biomolecules and inorganic components were formed on Zn surfaces during immersion in both the whole blood and plasma. However, this phenomenon was not observed in the Ringer's and PBS. The same group also studied the mechanism of the protective layer formation in the whole blood by electrochemical measurement [21]. Long-term degradation profile of pure Zn in the whole blood was not yet carried out.

Blood plasma, which are neutral solutions containing inorganic components such as Na^+, Ca^{2+}, Cl^-, HCO_3^- and HPO_4^{2-} ions, as well as organic compounds like amino acids, glucose and proteins [22]. In the human blood serum, protein concentration is about 60~80 g L^{-1} [22], which is thought to have great influences on corrosion behaviour of implanted materials [23,24]. A number of previous studies have shown that in the presence of proteins biodegradable magnesium alloy display different corrosion behavior compare to that in the inorganic solutions [25–27]. Up to now, little information is known about corrosion behavior of Zn and its alloys under physiological conditions. Thus it is worthy to understand the influence of proteins on Zn corrosion. Bovine serum albumin (BSA) is a typical protein that has been widely used to simulate the protein in human body [28–32]. Herein, the

* Corresponding author.
E-mail address: luning.wang@ustb.edu.cn (L.-N. Wang).

https://doi.org/10.1016/j.corsci.2019.04.003
Received 10 December 2018; Received in revised form 19 March 2019; Accepted 1 April 2019
Available online 05 April 2019
0010-938X/

artificial plasma was prepared in the presence of 60 g L^{-1} BSA. Pure Zn was chosen for the tests with an aim to reduce the effects of other elements. The corrosion rate and corrosion products of pure Zn in artificial plasma was elucidated by immersion tests and electrochemical measurements. Profound understanding of surface reactions of pure Zn in vascular environments will encourage further exploration of biodegradation of Zn-based alloy and push forward efforts to make these materials applicable in biomedical stent.

2. Material and methods

2.1. Sample preparation

Zn foil with 99.99% purity was purchased from China New Metal Materials Technology Co. Ltd. The samples were cut into disks with diameter of 5 mm and thickness of 2 mm. All the samples were mechanically ground up to 5000 grit SiC sandpapers, mirror-polished with diamond abrasive paste, followed by rinsed in ultrapure water, acetone and ethanol successively to remove surface contaminants. The samples were then dried and stored in a drying vessel.

2.2. Immersion test

Corrosion behavior of Zn samples was carried out by in vitro immersion test in artificial plasma (denoted as "AP" in the following sections) up to 28 d. The chemical composition of the solution was selected from European Standard EN ISO 10993-15:2009 [33] and is indicated in Table 1. The pH of AP should be within 7.35–7.45 and adjusted with appropriated amount of 1 M NaOH or 1 M HCl. Each disk was immersed in 40 mL AP at 37 °C. The solution was renewed every day. The amount of released Zn ions into the solution was evaluated using an atomic absorption spectrophotometer (AAS, ThermoScientific M Series). The absorption spectra of the solutions were measured on a double beam Shimadzu UV–vis 2600 PC spectrophotometer. After different temporal intervals the samples were picked up, then washed with ultrapure water and dried before being weighted using a balance. The *weight loss* (W, mg cm^{-2}) was calculated using the following Eq. [34]:

$$W=\frac{m_i - m_f}{A} \quad (1)$$

where m_i is the initial weight of samples before immersion (mg), m_f is the final weight of each samples after cleaning the corrosion products (mg), A is the sample surface area exposed to solutions (cm^2). The corrosion products were removed in a chemical cleaning solution containing 100 g L^{-1} NH_4Cl for 2–5 min at 70 °C [35].

2.3. Surface analysis

Surface morphology of pure Zn after immersion was investigated by a field emission scanning electron microscope (FE-SEM, FEI Quanta 200) coupled with an Oxford Instrument INCA X-max^N-sight EDS analyzer. Fluorescence labelling of BSA was performed using fluorescein isothiocyanate (FITC). The conjugation reaction was carried out by adding the FITC to AP to the concentration of 6 mg/ml followed by an incubation process for 12 h at 4 °C in a dark environment. Fluorescence images were obtained using an IX71Fluoresce microscope (Olympus). Labelled BSA can emit a green light under the fluoresce microscope. To evaluate surface roughness of pure Zn at each immersion intervals, the surfaces were investigated using an atomic force microscope (AFM, Bruker Icon). The AFM images were rendered as 3D topography and the average surface roughness (R_a) of Zn surface over an area with 50 × 50 μm^2 was calculated using Roughness Icon (Nanoscope analysis 1.8). The cross-sectional images and elements of immersed sample was obtained by transmittance electron microscope (TEM, FEIF20). TEM sample was selected using focused ion beam (FIB, Zeiss Auriga) lift-out. The chemical composition in corrosion products was characterized by Fourier transform infrared spectrometer (FTIR, Nicolet 5700) in the wave number ranging from 1000–3500 cm^{-1}. X-ray diffraction (XRD) was conducted on the Smart Lab X-ray diffractometer (Rigaku) with Cu Kα radiation. Diffraction patterns were generated between 2θ values of 10-90°. Raman spectra between 400 and 1800 cm^{-1} were collected using a laser confocal Raman microscope (HR-800, Horiba). Raman scattering was excited by the 785 nm radiation of a diode laser. A 50× objective was used by collecting Raman data. X-ray photoelectron spectroscopy (XPS, PHI 5600) was used to characterize the surface chemical states of samples after immersion. The XPS spectra were recorded using Al Kα radiation (1486.6 eV) as excitation source.

Table 1
Chemical composition of the AP solution.

Chemical	Composition (g L^{-1})
NaCl	3.40
CaCl	0.10
KCl	0.20
$MgSO_4$	0.05
$NaHCO_3$	1.10
Na_2HPO_4 $12H_2O$	0.16
NaH_2PO_4	0.01
BSA (Bovine serum albumin)	60.00

2.4. Electrochemical measurements

Electrochemical measurements were performed by an electrochemical analyser (ModuLab XM). A three-electrode cell set-up was used wherein the pure Zn samples, saturated calomel electrode (SCE) and a platinum sheet were used as the working, reference and counter electrodes, respectively. For the working electrode, the backside of the square samples was connected with a copper wire and then sealed with epoxy to expose the research surface area of 1 cm^2. Open circuit potential (OCP) measurements were recorded for 1800s immersion. Potentiodynamic polarization (PDP) tests were conducted in a range of −0.1 V vs. OCP to −0.70 V vs. SCE at a constant scan rate of 1 mV s^{-1}. Electrochemical impedance spectroscopy (EIS) studies were carried out at OCP of 5 mV sinusoidal amplitude in the frequency range of 10^5 Hz to 10^{-1} Hz. The impedance data were analysed with the ZSimpWin software package and fitted to the equivalent curves. Linear polarization resistance (LPR) of the samples were measured at ± 20 mV vs. OCP with a potential sweep rate of 0.167 mV s^{-1}. All experiments were conducted at 37 ± 0.1 °C in AP.

In terms of electrochemical tests, the values of current density (i_{corr}) of pure Zn can be derived by the Stern-Geary Eq. (2):

$$i_{corr}=\frac{\beta_a\beta_c}{2.303\times(\beta_a+\beta_c)}\times\frac{1}{R_p} \quad (2)$$

For the samples without Tafel region in the anodic branches, the i_{corr} could be determined from the Eq. (3):

$$i_{corr}=\frac{\beta_c}{2.303}\times\frac{1}{R_p} \quad (3)$$

where the β_a and β_c are anodic and cathodic slope values. The R_p values obtained from LPR and EIS methods are denoted as R_{LPR} and $R_{p\text{-}EIS}$, respectively.

3. Results

3.1. Immersion test

3.1.1. Surface morphology and chemical composition

Fig. 1a–h portray SEM images of pure Zn immersed in AP for various intervals. In the case of magnified morphologies (Fig. 1a1–h1), points 1–24 are selected for EDS characterization. Grain boundaries are clearly

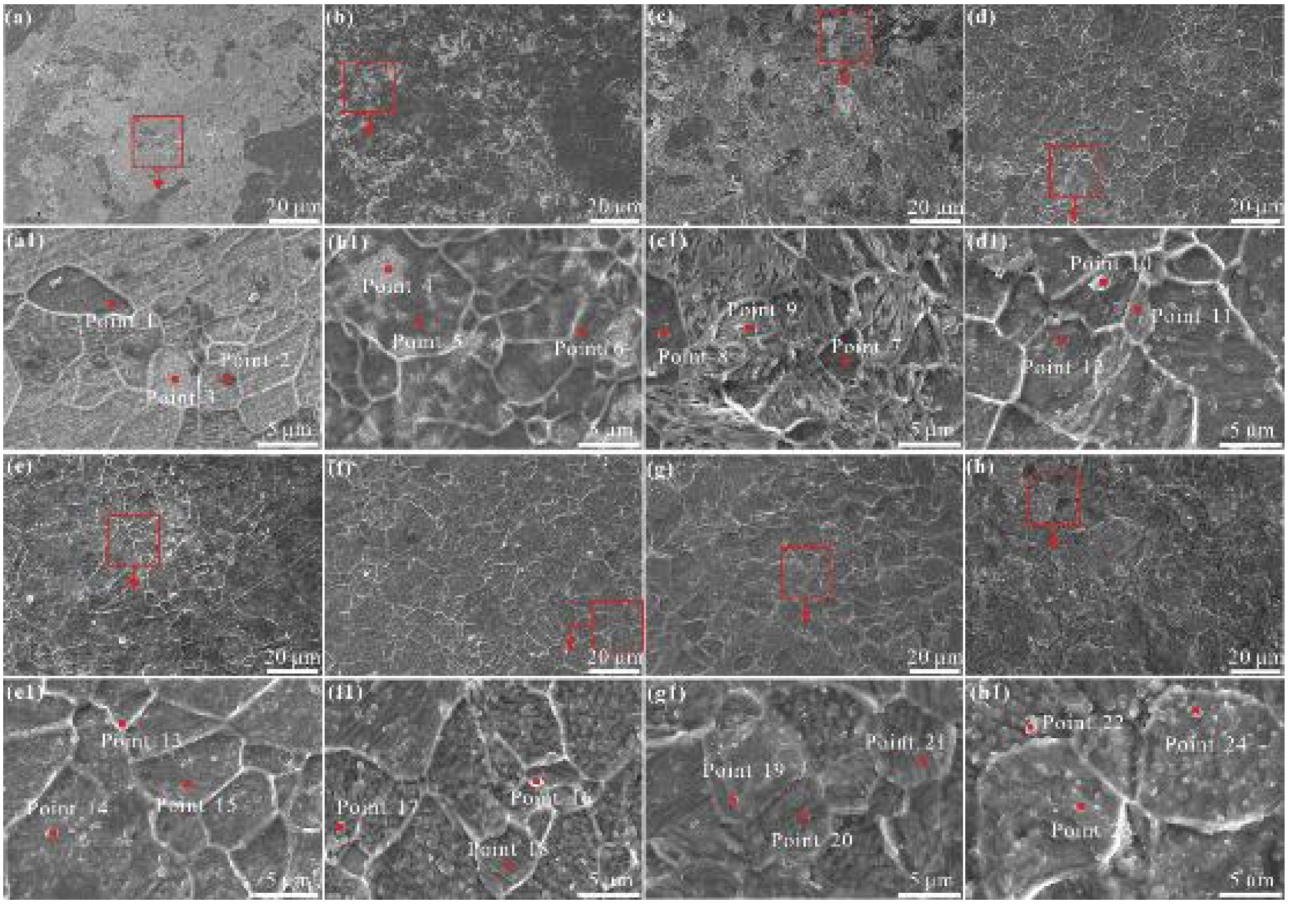

Fig. 1. SEM images of pure Zn after immersion in artificial plasma for (a) 0.5 d, (b) 1 d, (c) 3 d, (d) 5 d, (e) 7 d, (f) 14 d, (g) 21 d and (h) 28 d; (a1-h1) are enlarged morphologies of the selected areas in (a–h). Point 1 - Point 24 are selected for EDS point analysis.

observed on the surface after 0.5 d immersion (Fig. 1a) and turn out to be more pronounced with time (Fig. 1b–f). It has been reported that the grain boundaries with high-energy are preferred sites for corrosion initiation and proteins adsorption [28,36,37]. Scattered black aggregations also show up on the surface on 0.5 d and change into gel-like films that almost cover the surface (Fig. 1b). Then a number of oblate substances randomly appear on the surfaces with the extension of immersion time (Fig. 1c–f). Meanwhile, the grain boundaries become to be indistinct for 21 d immersion (Fig. 1g), and even almost disappear after soaking for 28 d (Fig. 1h).

The EDS analyses corresponding to the surfaces shown in Fig. 1 are listed in Table 2 and performed in Fig. 2. In Table 2, EDS data of every point confirms that the gel-like films (Fig. 1a1 and b1) and oblate substances (Fig. 1c1–h1) have higher content of elements C, O, N and S compared with that of surrounding flat areas, confirming the presence of BSA. With the extension of immersion time, the ratio of N to Zn for the BSA-containing substances keeps increasing, representing accumulation of BSA on sample surfaces. The atomic percentages of related elements for each immersion point are calculated based on point analyses (Table 2) and are shown in Fig. 2. The primary constituents formed on pure Zn surfaces mainly contain Zn, C, O, N, S elements. As time evolves, the percentage of Zn decreases continuously while C, O, N, S rise up obviously, which confirms the accumulation of BSA in the corrosion products.

To better analyse the spread of BSA on sample surfaces at different immersion time, fluorescence microscope was utilized. As shown in Fig. 3a and b, after 1 d immersion, large parts of sample surfaces are covered by BSA, which shows light green colour. During the next 2 d of immersion (Fig. 3c), almost the whole surface of pure Zn shows the green colour, indicating more BSA spreads on the surface. It is worth

Table 2
Elemental composition of the selected points marked in SEM images.

Immersion time	Points	Elemental composition (at.%)							
		Zn	C	O	N	S	P	Ca	N/Zn
0.5 d	1	64.3	32.8	1.4	1.2	0.1	0.2	0	0.02
	2	61.7	28.2	4.7	4.7	0.4	0.3	0	0.08
	3	68.2	28.7	2.8	0	0.1	0.2	0	0
1 d	4	61.6	33.4	2.2	2.6	0.2	0	0	0.04
	5	32.0	60.6	3.7	3.3	0.2	0.2	0	0.10
	6	38.4	54.6	4.1	2.5	0	0.3	0.1	0.06
3 d	7	51.4	39.2	5.8	3.0	0.3	0.3	0	0.06
	8	30.9	56.5	4.5	7.7	0.1	0.2	0	0.25
	9	29.2	58.7	4.5	7.2	0.2	0.3	0	0.25
5 d	10	31.8	56.3	4.5	7.0	0.2	0.2	0	0.22
	11	44.6	46.9	3.1	5.1	0.3	0	0	0.11
	12	28.9	59.0	5.0	6.7	0.2	0.2	0	0.23
7 d	13	12.8	66.9	8.5	11.4	0.1	0.2	0.1	0.89
	14	44.6	50.9	2.9	0.8	0.5	0.3	0	0.18
	15	44.2	47.7	3.2	4.3	0.3	0.3	0	0.09
14 d	16	21.4	59.3	7.8	10.9	0.4	0.2	0	0.51
	17	25.9	61.6	7.3	4.1	0.6	0.3	0.2	0.16
	18	35.1	56.0	5.3	2.8	0.5	0.1	0.2	0.08
21 d	19	16.7	60.8	10.5	10.8	0.6	0.4	0.2	0.65
	20	19.0	64.7	8.2	6.7	1.0	0.3	0.1	0.35
	21	15.7	63.5	8.9	10.7	0.8	0.3	0.1	0.68
28 d	22	12.4	66.2	8.6	11.5	0.9	0.4	0	0.93
	23	31.2	62.4	5.3	0	0.8	0.3	0	0
	24	18	63.2	6.4	11.7	0.4	0.3	0	0.65

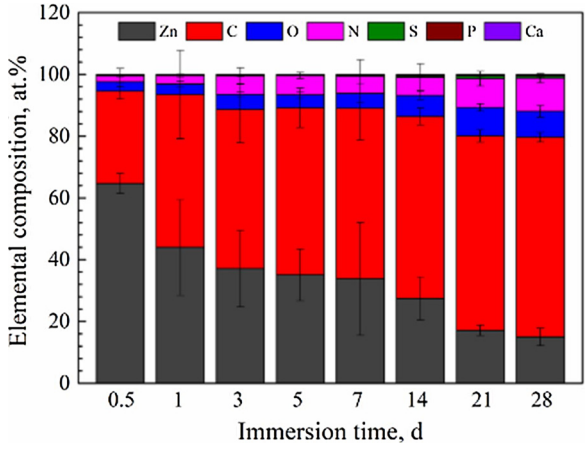

Fig. 2. Elemental composition of sample surfaces after immersion for different periods. (The data are calculated from Table 2).

noting that the grain boundaries show brighter green colour, which means more BSA absorb on the grain boundaries. On prolonging the immersion time, the sample surfaces display evident green colour and the grain boundaries become obscure (Fig. 3d–h). These changes suggest the accumulation of BSA on sample surfaces during the immersion. It also should be noted that there are some small areas (marked by white arrows in Fig. 3) showing the green colour with low intensity and even change into dark areas after 28 d immersion, which is caused by the contrast of adsorption amount of BSA on the surface. This phenomenon maybe because that these areas are the preferential sites to dissolve in the solution, which hinders the BSA adsorption. On the other hand, the conformation change after initial adsorption of BSA also affects the intermolecular forces and further interaction with sample surface [38].

Fig. 4 depicts the AFM images of pure Zn at each immersion intervals, also rendered as 3D plots. The sample surface presents globular features (Fig. 4a and a1), which are related to the BSA molecule aggregations and lead to an increase of surface height. After 1 d immersion grain boundaries apparently show up on the surface (Fig. 4b), resulting in an increase of R_a. The similar morphology is observed for the 3 d sample (Fig. 4c) except for a higher R_a value of 46.3 ± 1.0 nm (Fig. 4c1). It can be clearly seen that the grain boundaries are higher than the grains from the 3D images (Fig. 4a1–c1), implying more BSA adsorption on the grain boundaries in the initial immersion stage. This result is consistent with the fluorescence images and SEM images. Some aggregations appear on the 5 d sample surface, which could account for the increased R_a value of 97.8 ± 6.8 nm (Fig. 4d1). And after 7 d most parts of the grain are occupied by BSA-containing structures (Fig. 4e), resulting in an increase of R_a. The sample surfaces show similar morphologies after immersion for 14 d. The grain boundaries gradually disappear with time (Fig. 4f–h) and the R_a values continue to rise up (Fig. 4f1–h1). It can be deduced that the metal matrix dissolute sustainably and at the same time the BSA-containing corrosion products accumulate constantly on the surfaces, resulting in the increase of R_a value during the immersion.

Fig. 5 shows the cross section image acquired by TEM and corresponding EDS maps of pure Zn after immersion for 28 d. In Fig. 5a, it is evident that the corrosion product layer covers the sample surface unevenly. And the thickness ranges from about 550 nm for Section I to 150 nm for Section II. The EDS mappings of Fig. 5b–d display that the corrosion products are mainly comprised of C and O, which are originated from BSA molecules.

Fig. 6a shows XRD patterns for Zn samples after immersion in AP for various periods. In addition to the peaks from Zn substrates, no more diffraction peaks can be observed on the XRD spectra of all samples. This can be ascribed to that the corrosion products have amorphous structures.

The FTIR spectra as shown in Fig. 6b provides information about organic groups in the corrosion layers. According to the literature, in the absence of Zn^{2+} ions, the amide I (C═O) region for BSA shows four main peaks at 1674, 1661, 1644 and 1628 cm^{-1}, the bands at 1661 and 1611 cm^{-1} can be assigned to α-helical segment of BSA, the bands at 1674 and 1628 cm^{-1} can be assigned to β-sheet and turn segment of BSA [39]. Herein, the peaks for amide I emerges into one peak at 1652 cm^{-1}. The peak shifting indicates that Zn^{2+} binding occurs mainly through BSA carbonyl groups. Additionally, the peak at 1548 cm^{-1} is attributed to the amide II (N−H bending and C–N stretching) of CONH. The absence of BSA amide II peak at 1537.8 cm^{-1} [39] indicates that Zn^{2+} binding is also through C–N groups. The intensity of amide II peak evidently increases after immersion for 3 d. This could be related to accumulation of BSA on the surfaces. Peaks at 2922 and 2855 cm^{-1} are attributed to stretching vibrations of C–H groups from BSA. In Fig. 6, there are two identifiable trends: (1) the intensities of the peaks at 2922 and 2855 cm^{-1} decrease with immersion time, (2) the intensities of the peaks at 1652 and 1548 cm^{-1} increase with immersion time. These features suggest that more BSA accumulates on sample surfaces with increasing immersion time.

The Raman active groups in BSA consist of various amide groups and aromatic side chains such as tyrosine (Typ), tryptophan (Try) and phenylalanine (Phe). The interaction of BSA and pure Zn surfaces was also testified by the Raman spectra (Fig. 6c). The characteristic peaks for BSA were detected at around 511, 847, 947, 1001, 1112, 1441 and 1650 cm^{-1} (the black line). Details of the band positions and their assignments are reported in Table 3. The pure Zn surface after immersion in AP also show the bands for BSA (the red line), which is indicative of the appearance of BSA on sample surface. It is notable that all the bands shift towards high wavenumbers after immersion, which testifies the combination of BSA and Zn surface.

The XPS survey spectra of pure Zn samples after soaking for different times are presented in Fig. 7. The peaks for Na1 s and Cl 2 s are detected on the sample surface after 0.5 d immersion. This result is attributed to the adhesion of NaCl from AP solution. There is no difference in chemical compositions of the corrosion products, which mainly consists of Zn, N, C and O elements (Fig. 7a). In Fig. 7b, some peaks for Ca 2p, P 2p, S 2 s and S 2p are also detected. The existence of S element confirms the formation of species containing BSA on sample surfaces. Additionally, high-resolution XPS spectra of C 1 s and N 1 s on typical sample surfaces are collected and the corresponding results are listed in Table 4. The C 1 s spectrum signalised a new peak around 285.8 eV after 14 d (Fig. 8a). Fig. 8b and c designate the curve fits of the C 1 s spectra for the samples after immersion for 1 d and 28 d, respectively. The peaks are well fitted with five contributions at 284.5 eV, 285.4 eV, 286.2 eV, 287.5 eV and 288.3 eV. The low-binding-energy signal is assigned to C–H/C−C bonds, whereas the high-binding-energy signals are respectively assigned to C–N, C–O, C═O and O = C–N. Generally, the peak at 286.2 eV is assigned to NH − CHR − CO carbons of the protein backbone and the peak at 288.3 eV is assigned to the − CO-NH- peptide bonds of proteins [45,46]. Thus, these characteristic bonds indicate the presence of BSA on sample surfaces. Apparently, the appearance of a new peak at 285.8 eV is caused by the increase in C–N and C–O intensity. The proportion of C–N increased from 0.20 to 0.22 and the C–O increased from 0.16 to 0.22. Fig. 8d shows that the N 1 s peaks shifted towards low binding energy after 14 d. The deconvolution of N 1 s spectra (Figs. 8e and f) reveal two components, centred at 399.4 eV and 400.0 eV, which correspond to the C–N and C═O−NH bonds [47,48], as expected for the amine or amide groups of BSA [46]. According to other researchers, the peaks at around 399.0 eV also represent the C−N−Me groups [49,50]. The proportion of C–N bonds increases from 0.33 to 0.56, which accounted for the shift of N 1 s peak. The increased intensity of C–N in both C 1 s and N 1 s spectra may be relative to the accumulation of Zn^{2+} or $ZnO/Zn(OH)_2$ on the surface, in accordance with the results from FTIR spectra.

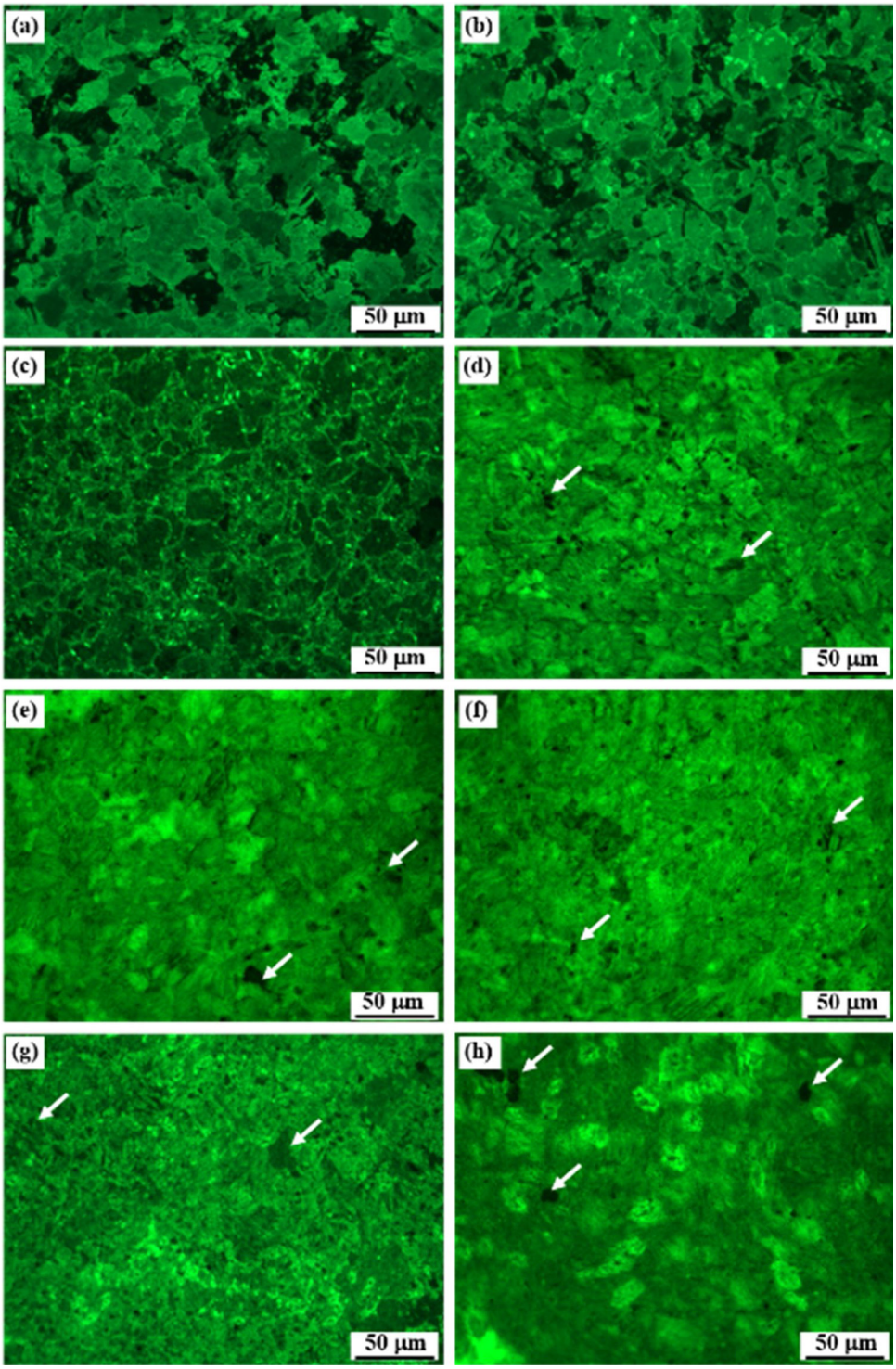

Fig. 3. Fluorescence microscope images of labeled BSA with FITC on pure Zn sample surfaces after immersion in AP for different time: (a) 0.5 d, (b) 1 d, (c) 3 d, (d) 5 d, (e) 7 d, (f) 14 d, (g) 21 d, (h) 28 d. Arrows indicate typical dark areas.

XPS depth profile was conducted on the sample immersed for 14 d. The rate of sputtering was about 20 nm min^{-1}. Fig. 9a exhibits the atomic concentration change as a function of sputtering time. It is noticed that at the end of 4 min, there is little element O and small variations are detected for other atomic concentrations. Assuming the etching rate to the surface material is uniform, the thickness of the corrosion layer is around 80 nm. From the outer surface to inner, the concentration of C element, which is originated from BSA, decreases obviously, whereas the concentration of Zn increased rapidly. However, the element P is only detected at the outer surface and the concentration of Ca is relatively low at different depth. We can speculate that there is no corrosion products rich in Ca and P elements.

Fig. 9b–d and g show the XPS depth sputtering spectra of C 1 s, N 1 s, O 1 s and Zn $2p_{3/2}$. The peak intensities decrease with sputtering time except an increment for Zn $2p_{3/2}$. With respect to O 1 s spectra, the peak is composed of four contributions at 530.1 eV, 531.2 eV, 532.0 eV and 532.5 eV (Fig. 9e and 9f), which represented O^{2-}, OH^-, O═C–N and H_2O [51,52]. In addition to the decrease of O = C–N, the

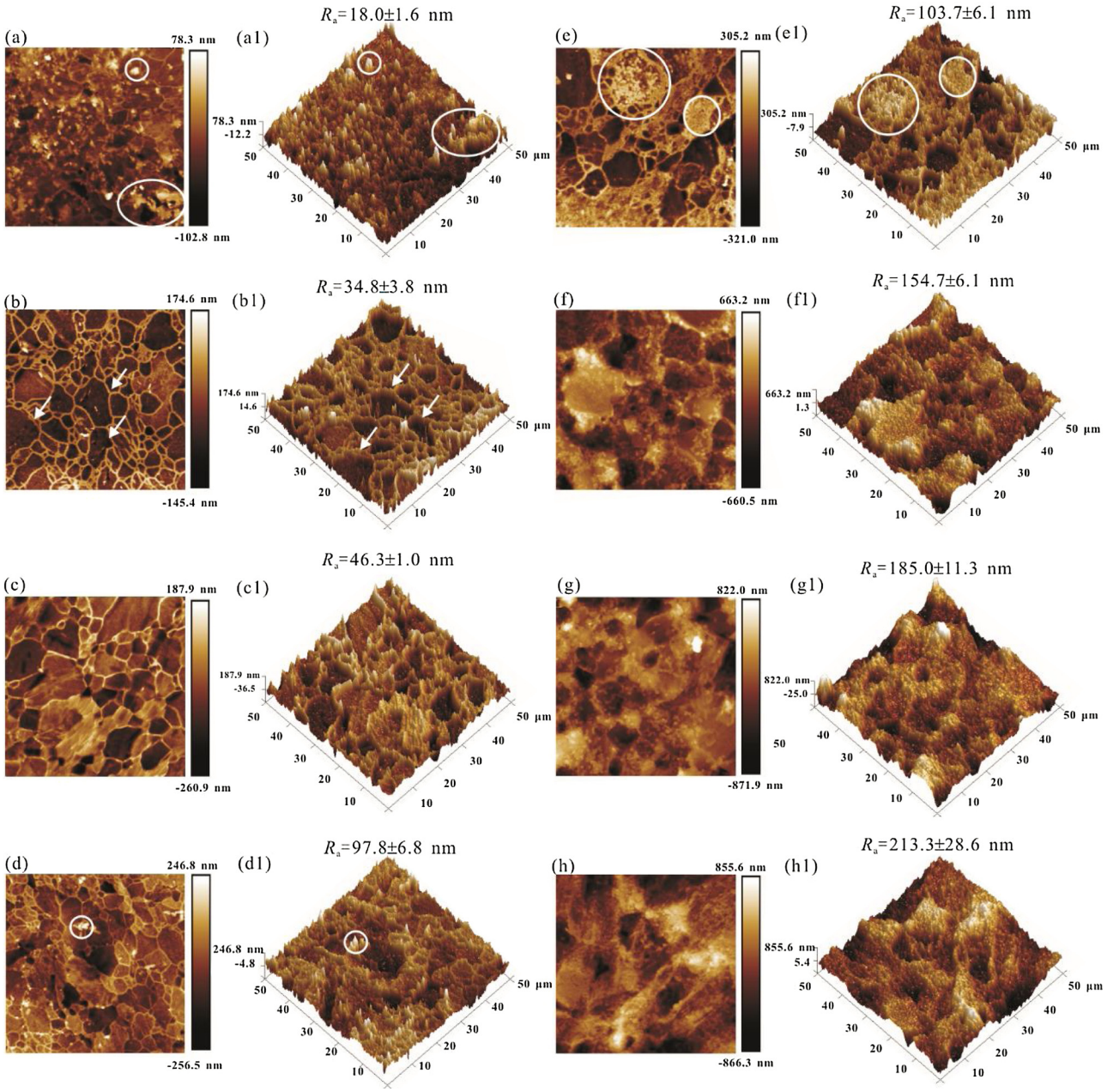

Fig. 4. AFM images of pure Zn at different immersion time: (a, a1) 0.5 d, (b, b1) 1 d, (c, c1) 3 d, (d, d1) 5 d, (e, e1) 7 d, (f, f1) 14 d, (g, g1) 21 d, (h, h1) 28 d. (a1-h1) are corresponding 3D images. The arrows indicate the grain boundaries and white circles indicate the aggregations at different immersion time.

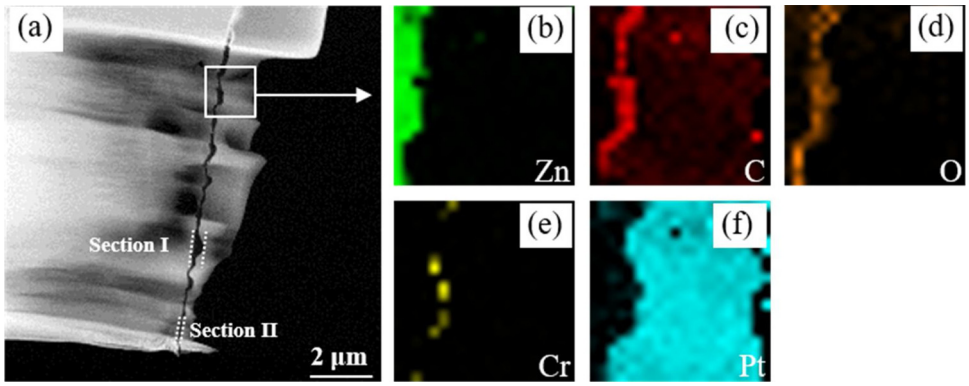

Fig. 5. (a) TEM image of cross section of pure Zn after immersion in AP for 28 d, (b–f) the corresponding elemental mapping images of the square area in the image (a). Section I and Section II are chosen for the thickness measurement.

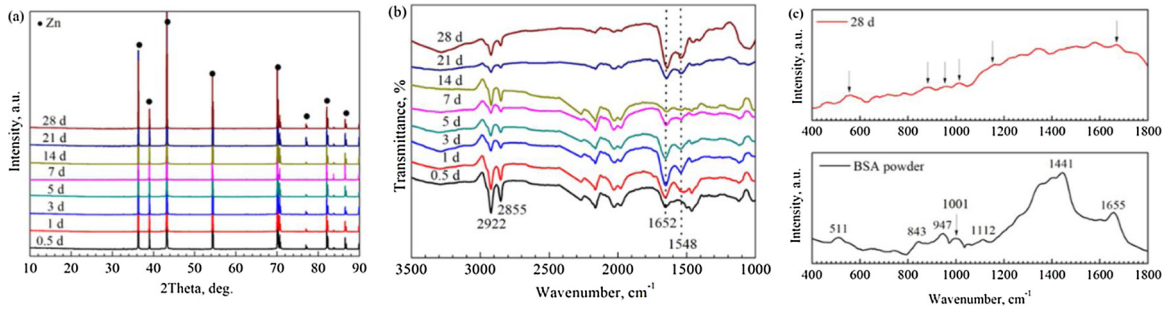

Fig. 6. (a) XRD patterns and (b) FTIR spectra of pure Zn sample surfaces after immersion in AP for different time; (c) Raman spectra of BSA (the black line) and pure Zn after immersion for 28 days (the red line) (For interpretation of the references to colour in this figure legend, the reader is referred to the web version of this article).

Table 3
Raman band used as molecular species-specific fingerprint and corresponding vibrational modes.

Raman band (cm^{-1})	Assignments	References
511	S-S stretching mode	[40]
843	Tyr	[40,41]
947	skeletal C-C vibration	[40,41]
1001	Phe	[41,42]
1112	Tyr	[40,41]
1441	CH_2 vibrations	[43]
1655	Amide I	[41,44]

Table 4
Results obtained from deconvoluted XPS spectra of C 1 s, N 1 s, O 1 s, Zn $2p_{3/2}$ on pure Zn surfaces.

Element	Characterized bonds	Binding energy (eV)	References
C 1 s	C-H/C-C	284.5	[45,46]
	C-N	285.4	[45,46]
	C-O	286.2	[45,46]
	C = O	287.5	[45,46]
	O = C-N	288.3	[45,46]
N 1 s	C-N(-Me)	399.4	[46,47,48,49,50]
	C = O-NH	400.0	[46,47,48]
O 1 s	O^{2-}	530.1	[51,52]
	OH^-	531.2	[51,52]
	O = C-N	532.0	[51,52]
	H_2O	532.5	[51,52]
Zn $2p_{3/2}$	1021.6	Zn/ZnO	[53]
	1022.7	$Zn(OH)_2$	[53]

proportion of OH^- increases from 0.51 to 0.75. The OH- peak is originated from both hydroxides in the corrosion layer and hydroxyl groups in the BSA molecules, whereas the O^{2-} peak is attributed to zinc oxide. As exhibited in Fig. 9h and i, Zn $2p_{3/2}$ spectra is composed of two contributions centred at 1021.6 and 1022.7 eV, which represent Zn/ZnO and $Zn(OH)_2$ [53]. Combined with the results from O 1 s spectra, Zn element thus exists in the corrosion layer in the form of ZnO and $Zn(OH)_2$. As the detection depth increases, zinc oxides gradually change to zinc substrate.

3.1.2. Ion Dissolution and weight loss measurements

As depicted in Fig. 10a, in the first 7 d the daily release amount of Zn^{2+} gradually increases except for a flexion point around day 3, then decreases slowly during 7–21 d, and inversely witness an upward trend in the few days later. Overall, the release amount of Zn^{2+} varied between 0.13 and 0.36 mg L^{-1}. As depicted in Fig. 10b, the weight loss of Zn samples increases steadily with time, ascertaining the dissolution of pure Zn in the AP.

3.1.3. Micrographs of corroded Zn sample

Fig. 11 provides representative SEM images of pure Zn after removal the corrosion products so as to unveil the underneath corrosion attack. The grain boundaries are obvious before 14 d immersion (Fig. 11a–c) and become obscure at 28 d. Fig. 11c1 and d1 show the enlarged areas of 14 d and 28 d samples. It can be seen that some tiny pores (marked by the arrows) show up on the surfaces. These pores may originate from the defects of the surfaces during the preparation, or because the impurities act as the anode and thus lead to the galvanic corrosion in these micro areas. Overall, no severe localized corrosion pits are observed throughout the immersion.

3.2. Electrochemical measurements

Fig. 12a performs the typical OCP curves of Zn during the test in the electrolytes. OCP value keeps relatively stable for the 0 d and 0.5 d immersion samples. After 1 d immersion the OCP value of pure Zn undergo small fluctuations throughout the tests. The evolution of OCP, the values at which EIS measurements are carried out are summarized in Fig. 12b. It is obvious that the OCP value increases from −1.12 V/

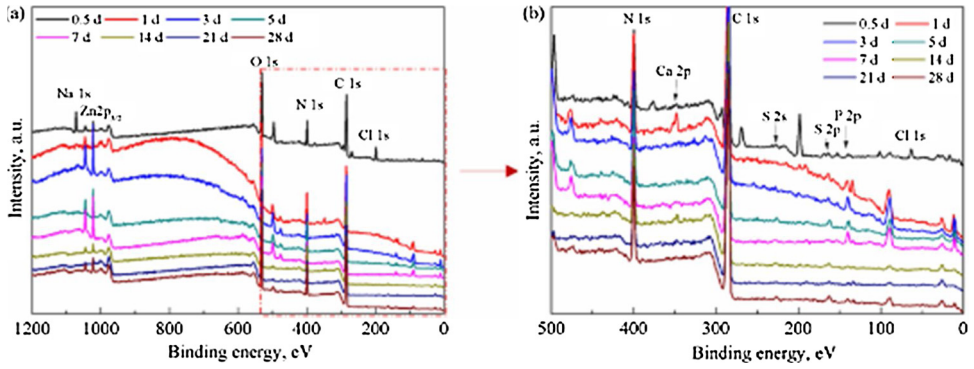

Fig. 7. XPS spectra of Zn after immersion in AP for different time: (a) XPS survey; (b) fragment of XPS survey from 500 eV to 0 eV.

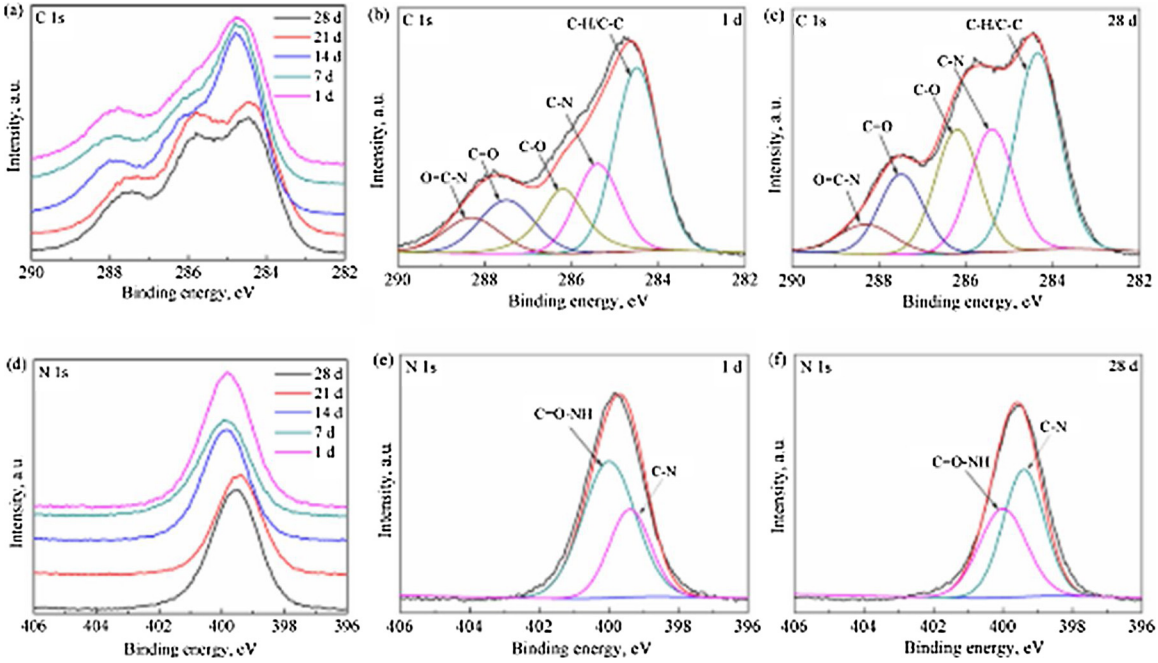

Fig. 8. XPS spectra of Zn after immersion in AP for different time: (a) C 1 s region and (b, c) high-resolution spectra of C1 s for 1 d and 28 d, respectively; (d) N 1 s region and (e, f) high-resolution spectra of N1 s for 1 d and 28 d, respectively.

SCE for 0 d to −1.04 V/SCE for 0.5 d and rise to −0.98 V/SCE for 1 d. Small variations are detected for the 3–7 d immersion samples. Then a slight increase of OCP value is observed after 14 d. It is obvious that all the OCP values after immersion are higher than that at 0 d. This behavior may refer to the constant buildup of corrosion products on sample surfaces, which decrease the corrosion susceptibility of pure Zn in the AP.

Fig. 13 compares the PDP curves corresponding to pure Zn at each immersion time points. Corresponding parameters including corrosion potential (E_{corr}), i_{corr}, β_a and β_c slopes are shown in Table 5. In Fig. 13a, a passivation-like behavior (below −0.92 V/SCE) in the anodic branch is detected for 0 d and 0.5 d samples and vanishes after longer immersion time, which may result from the adsorption of BSA onset of the immersion and subsequent desorption. After 5 d immersion, small passivation area emergences (Fig. 13b). This behavior could be related to the accumulation of metal oxides and BSA on the sample surfaces during the immersion. It also can be seen that the anodic and cathodic current densities at the same potential reduce greatly within 1 d immersion, then obvious increases are observed over 3 d. However, the current densities start to reduce again after 7 d. As listed in Table 5, the value of E_{corr} is shifted toward positive values with immersion time except for a small fluctuation. The i_{corr} values show the same trend as the anodic current densities. And after 28 d, the immersed pure Zn displays better corrosion resistance than the sample without immersion (0 d). The results reflected in Table 5 indicate that both anodic and cathodic Tafel slopes are changed during the immersion. This phenomenon reveals that the corrosion products have an impact both on the dissolution of pure Zn and oxygen consumption.

Fig. 14 shows the EIS spectra of pure Zn after immersion for different time. From the results of Nyquist plots, a Warburg impedance character is observed in the low frequency region for the samples immersed within 3 d (Fig. 14a). After that, the Warburg impedance character disappears. The diameters of capacitive loop show an increase within 1 d immersion, then decrease during the immersion for 3–7 d and increase again after 7 d, which shows the same trend as the impedance modulus, |Z| at the lowest frequency (Fig. 14c). It is well consistent with the results of PDP curves (Fig. 13). The Bode plots show that there are two overlapped time-constants in medium and low frequency regions for pure Zn after immersion for different times.

A two-time constant model with the Warburg impedance is used to fit the EIS data of pure Zn within 3 d immersion. As shown in Fig. 14e (insertion in Fig. 14a), R_s represents the solution resistance, R_f and CPE_f describe the first capacity loop at medium frequency, which represent the film resistance and capacity, respectively. R_{ct} and CPE_{dl} are used to describe the second capacity loop at low frequency, which represents the charge transfer resistance and the electric double layer at the metal/electrolyte interface. CPE is a constant phase element and is employed here to compensate the non-homogeneity in the system [54]. The electrical impedance of a CPE can defined as [23]:

$$Z_{CPE}=\frac{1}{(j\omega)^{n}Y_0} \quad (4)$$

where Y_0 is the general admittance function and ω represents the angular frequency. The exponent n is a coefficient related to deviation from pure capacitance. A two-time constant model in Fig. 14f (inset in Fig. 14b) is used to fit the EIS data of pure Zn without immersion (0 d) and over 5 d immersion. The fitting parameters are listed in Table 6. The chi-square values (χ^2) are less than 4×10^{-3}, indicating a satisfactory fit between the measured and simulated values.

During the immersion for the first 1 d, the value of R_f increases gradually, which indicates that the adsorption of BSA protects the sample from corrosion. However, during the immersion for 3–7 d, R_f decrease gradually and then greatly increase again after 7 d. A reverse trend is identified in the terms of admittance for CPE_f which denotes that the corrosion product layer become thicker [55]. It is obvious that R_{ct} values almost show the same trend as R_f. In the EIS measurements, the polarization resistance $R_{p\text{-}EIS}$ can be obtained by combination of R_{ct} and R_f [56]. The value increases with time in the first 1 d and decreases within 7 d, then goes up consistently as time progresses, signifying the corrosion resistance of pure Zn is improved after immersion for longer time. This result is well corresponding to that of PDP curves.

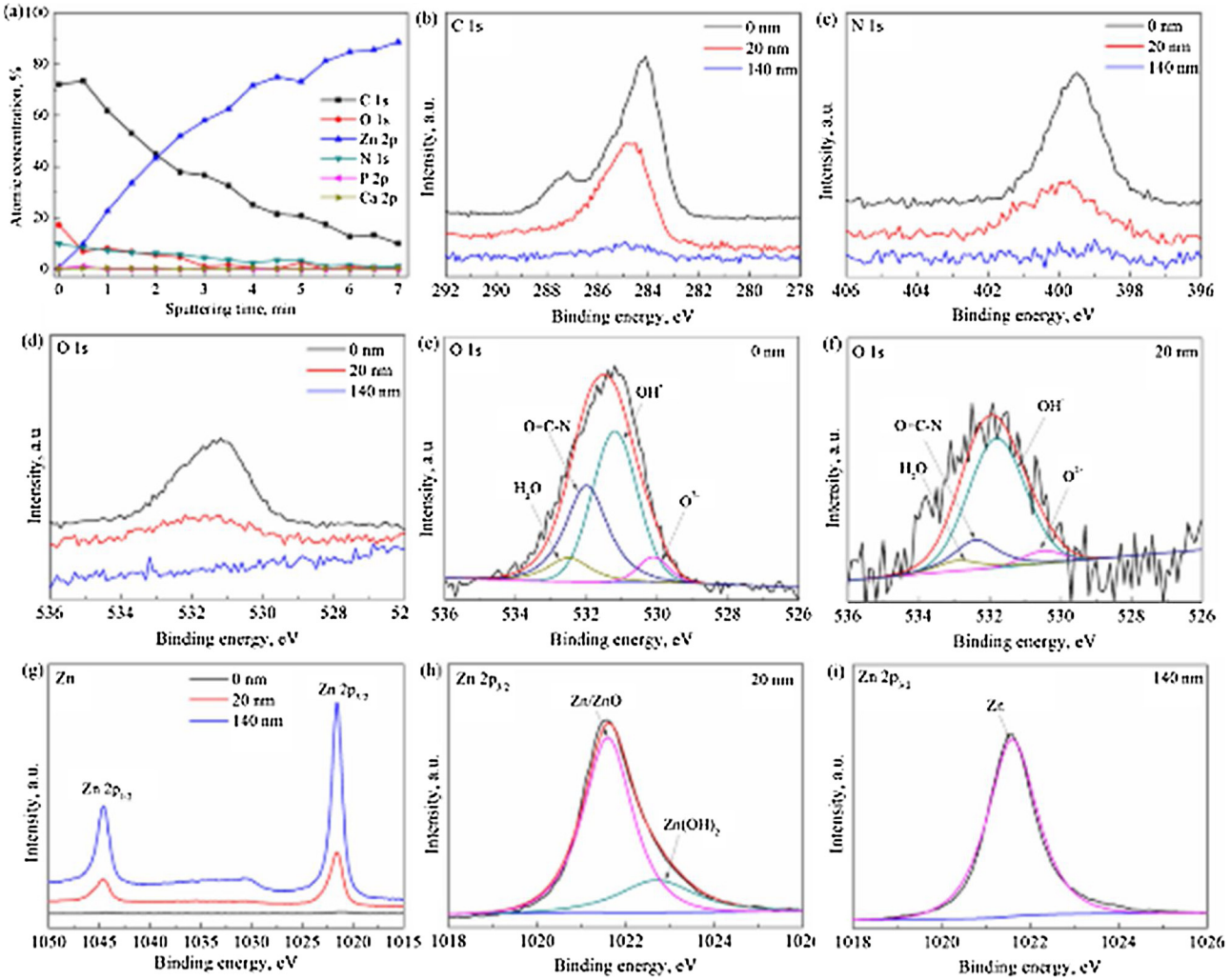

Fig. 9. XPS spectra of pure Zn immersed in AP for 14 d: (a) depth profile of elemental concentrations, (b) C 1 s region, (c) N 1 s region, (d) O 1 s region, (e, f) high-resolution spectra of elements O 1 s, (g) Zn $2p_{3/2}$ region and (h, i) high-resolution spectra of Zn $2p_{3/2}$.

4. Discussion

4.1. The influence of BSA on the corrosion behavior

The pure Zn immersed in AP encounters uniform corrosion, but other works reported that pure Zn undergoes severe localized corrosion with massive corrosion products [16,17,57]. The differences come from various initial states (being polished or only mechanically ground by SiC papers) of sample surfaces or the different components among test solutions (whether containing organic components or not). In order to get insight into the influence of BSA on the corrosion behaviour of pure Zn, the corrosion in revised simulated body fluid (r-SBF) in our previous work [58] are used here as a comparison.

In the r-SBF, corrosion products on the pure Zn are mainly consisted of inorganic components, namely $Zn_3(PO_4)_2$ and $Zn(OH)_2$/ZnO close to the substrate and $Ca_3(PO_4)_2$ and $CaHPO_4{\cdot}2H_2O$ on the top surface. After 10 d immersion, the corrosion layer is compact with thickness over 2 μm. However, the corrosion products on pure Zn are mainly

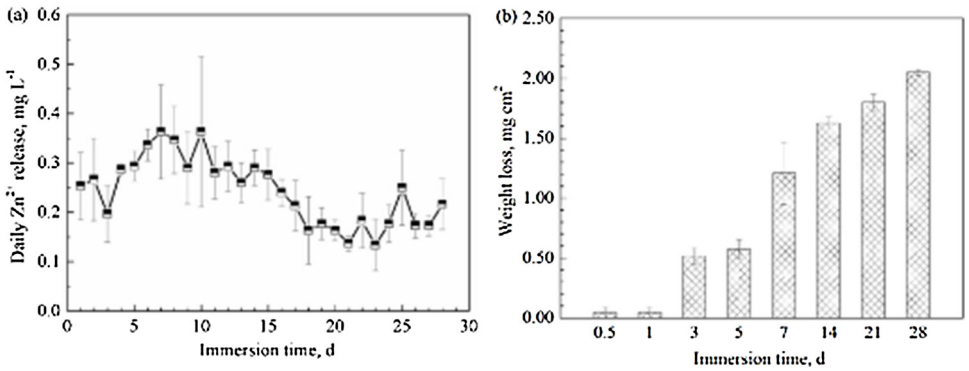

Fig. 10. (a) Daily Zn^{2+} release amount and (b) weight loss of Zn samples during the immersion in AP for 28 d.

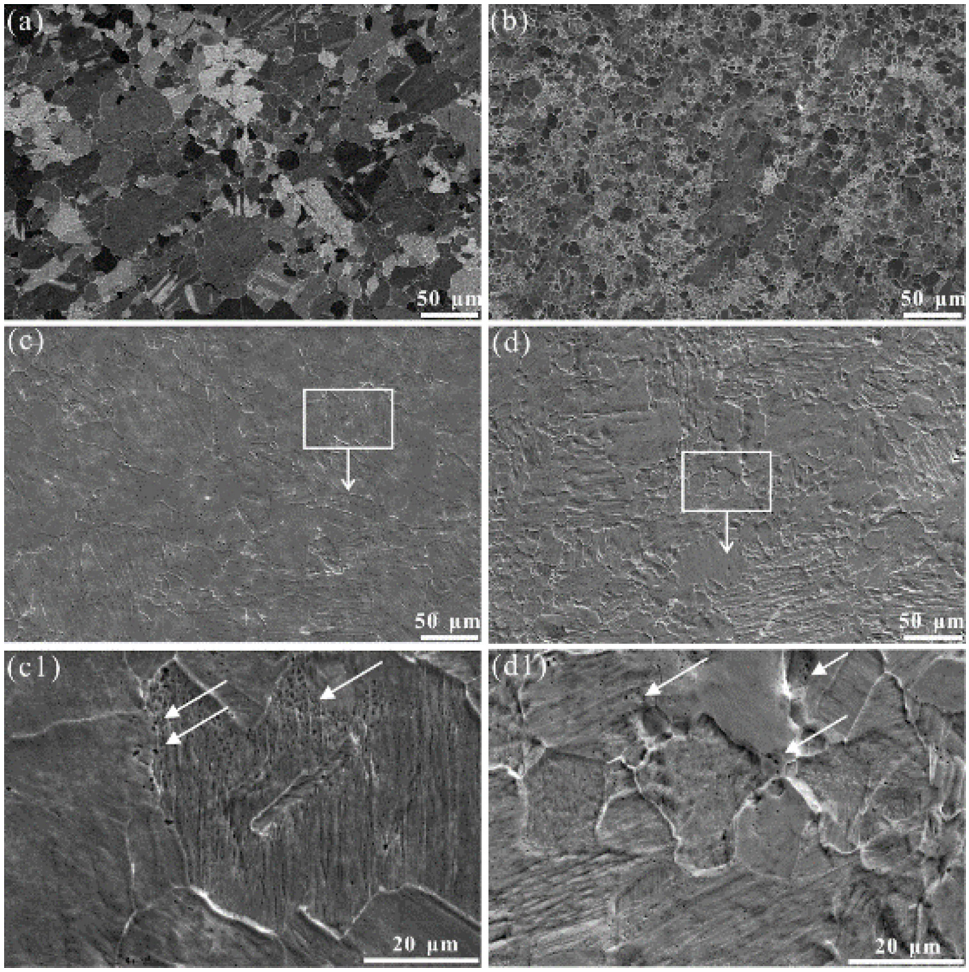

Fig. 11. SEM images of pure Zn after removal the corrosion products on the surfaces: immersion in AP for (a) 1 d, (b) 7 d, (c) 14 d and (d) 28 d. (c1 and d1) are enlarged areas of (c and d). Arrows indicate the tiny pores on sample surfaces.

comprised of BSA and $ZnO/Zn(OH)_2$ after immersion in the AP. This result can be rationalized that the presence of BSA hiders the formation of inorganic compounds. However, as reported by Yang et al [15], in the in vivo study the corrosion products on pure Zn stent are comprised of Zn, O and P elements after 1 month. It should be note that there are other organic substances such as cells [59] and glucose [60] in the whole blood that may interfere with the corrosion of implanted biomaterials. In addition, the circulation of blood in the body could also influence the corrosion of pure Zn.

In the electrochemical tests, a comparison of parameters within 14 d obtained in r-SBF and AP are shown in Fig. 15. Interestingly, in the presence of BSA the i_{corr} and R_p show almost completely opposite trends compared with the data for r-SBF. Generally, BSA accelerates the corrosion rate of pure Zn at first and then suppress the corrosion till 14 d except for 0.5 and 7 d. One should note that the i_{corr} values here are obtained from the Stern-Geary equation, while that in the r-SBF are obtained by the Tafel extrapolation. The discrepancy of calculation methods should be taken into consideration. Additionally, from the polarization curves one can observed that in the first 6 h immersion in r-SBF, pure Zn only displays small passivation-like regions (the figures are not shown here). However, in the presence of BSA in this work distinct passivation areas show up for 0 d and 0.5 d samples. This difference implicates that the rapid adsorption of BSA alters the corrosion behavior of pure Zn in the initial of immersion.

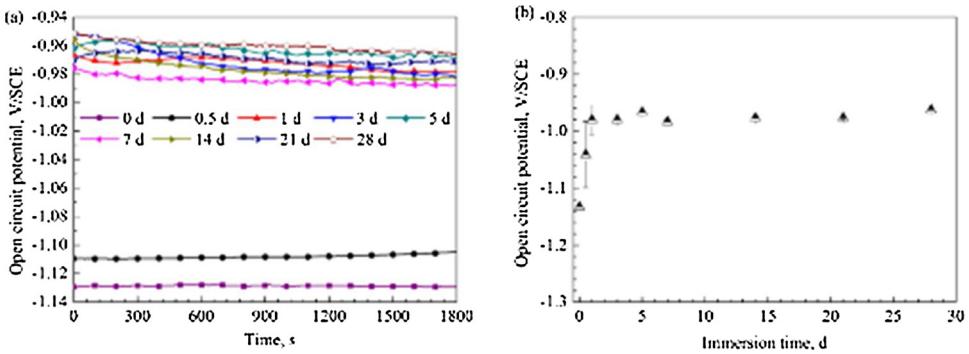

Fig. 12. (a) OCP evolution with time in the electrolytes, (b) OCP values of pure Zn as a function of immersion time.

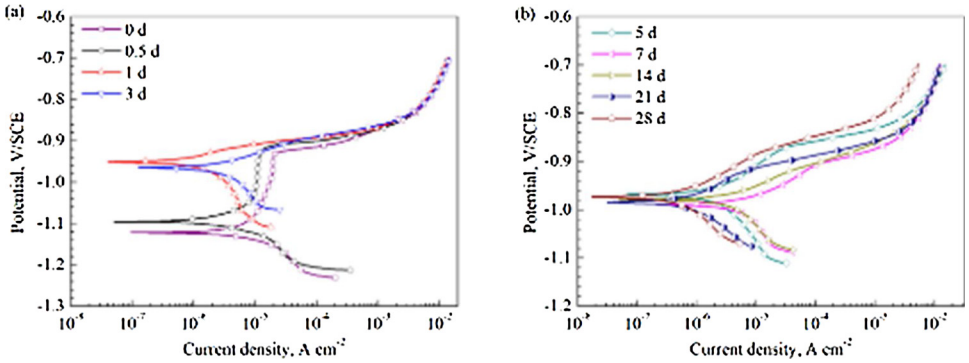

Fig. 13. PDP curves of pure Zn after immersion in AP for different time: (a) 0 d, 0.5 d, 1 d and 3 d, (b) 5 d, 7 d, 14 d, 21 d and 28 d.

4.2. Corrosion rate calculation

In the immersion test, the corrosion rate (CR_w, μm y^{-1}) of pure Zn derived from weight loss can be calculated according to ASTM G31-72 [34]:

$$CR_w = 87.4 \times \frac{W}{A \cdot D \cdot t} \quad (5)$$

where D is the material density (g cm^{-3}) and t the immersion time (h). Corrosion rate (CR, μm y^{-1}) corresponding to electrochemical tests can be calculated as follows [51]:

$$CR = 3.15 \times 10^5 \frac{a i_{corr}}{NFD} \quad (6)$$

The component a is atomic weight (g mol^{-1}), N the number of equivalent exchange and F the Faraday's constant. The corrosion rates obtained by LPR and EIS methods are denoted as CR_i and CR_{EIS}, respectively. The calculated data are listed in Table 7. The current density obtained from LPR and EIS measurements decrease apparently in the first 1 d and increase to 5.83 ± 0.63 and 6.79 ± 1.13 μA cm^{-2} respectively after 7 d, then exhibit a decreasing trend till 28 d. The corrosion rates are changing in the same order as the current density, while the polarization resistances display a reverse trend. This suggests that the BSA adsorption film cannot provide sufficient protectiveness for pure Zn in the initial stage and that the accumulated corrosion products in the later stage can protect samples effectively. In terms of CR_w, the values are much smaller than CR calculated from the LPR and EIS methods in the first 14 d. The reason is likely that the electrochemical measurements are carried out under applied current, which can accelerate the corrosion rate, especially for the metal with exposed surface. According to the Eq. (6), the difference between CR_i and CR_{EIS} is caused by the different methods to get the impendence values. Once the corrosion products are formed, they act as a physical barrier. Thus the charge transfer will be impeded, leading to the reduction of corrosion rate in the electrochemical tests. As for the weight loss method, the material is examined under natural condition in the solution. The CR_w is quite close to the real condition and is relatively reliable compared to CR_i or CR_{EIS}. Although different values of CR were obtained by three methods, the variation tendency of values disclose similarity during the immersion. After 21 days, the corrosion rates are close and finally give the values of 16.52 ± 0.21, 11.31 ± 2.79, 12.44 ± 5.37 μm y^{-1} for 28 days, respectively. These results are close to 20 μm y^{-1} design criteria. On the other hand, the corrosion rates in this work is similar to the in vivo results reported by Bowen et al [2]. It can be concluded that the artificial plasma used here is a good choice for in vitro test of stent materials.

From a viewpoint of biodegradation, the service life of stents in the body should be taken into account. By hypothesizing a stent made of pure Zn with a wall thickness of 100 μm for cardiovascular artery, and the corrosion initiates from both sides of the stent wall, the stent will be totally degraded in 3 years according to the values of CR_w (16.52 ± 0.21 μm y^{-1}). It should be pointed out that the corrosion rates of pure Zn wires in vivo rise up consistently with the implantation time [2]. Therefore, a long-term in vitro immersion test is necessary to better understand the degradation profile of pure Zn in the blood.

4.3. Corrosion mechanism of pure Zn in BSA-containing AP

According to the results interpreted in previous, the corrosion mechanism of pure Zn in AP can be divided into three stages as shown in Fig. 18. During the immersion, dissolution of pure Zn takes place according to the Eqs. (7) and (8):

$$\text{Anodic reaction: } Zn \rightarrow Zn^{2+} + 2e^- \quad (7)$$

$$\text{Cathodic reaction: } O_2 + H_2O + 4e^- \rightarrow 4OH^- \quad (8)$$

The Pourbaix diagram for Zn shows that Zn has a tendency to be passivated to $Zn(OH)_2$ under neutral or slightly alkaline conditions [61], parts of which was likely dehydrated to form ZnO [62]. The chemical reactions are as follows:

$$Zn^{2+} + 2OH^- \rightarrow Zn(OH)_2 \quad (9)$$

$$Zn(OH)_2 \rightarrow ZnO + H_2O \quad (10)$$

Table 5
Electrochemical parameters of pure Zn after immersion in AP for different time.

Immersion time	β_a (mV dec^{-1})	$-\beta_c$ (mV dec^{-1})	E_{corr} (V/SCE)	i_{corr} (μA cm^{-2})
0 d	–	81.40 ± 5.38	−1.12 ± 0.01	10.53 ± 1.57
0.5 d	–	45.36 ± 4.60	−1.09 ± 0.05	6.46 ± 0.48
1 d	38.29 ± 2.43	89.04 ± 8.64	−0.94 ± 0.02	2.12 ± 0.30
3 d	58.11 ± 8.79	86.60 ± 9.34	−0.96 ± 0.02	3.42 ± 0.62
5 d	81.07 ± 3.49	125.20 ± 16.03	−0.97 ± 0.02	3.62 ± 0.33
7 d	47.55 ± 7.79	105.70 ± 8.05	−0.98 ± 0.01	5.83 ± 0.63
14 d	50.87 ± 2.40	108.63 ± 6.69	−0.98 ± 0.01	4.99 ± 0.23
21 d	57.88 ± 9.36	121.23 ± 16.60	−0.98 ± 0.02	1.04 ± 0.35
28 d	64.80 ± 12.46	156.30 ± 44.59	−0.97 ± 0.01	0.76 ± 0.18

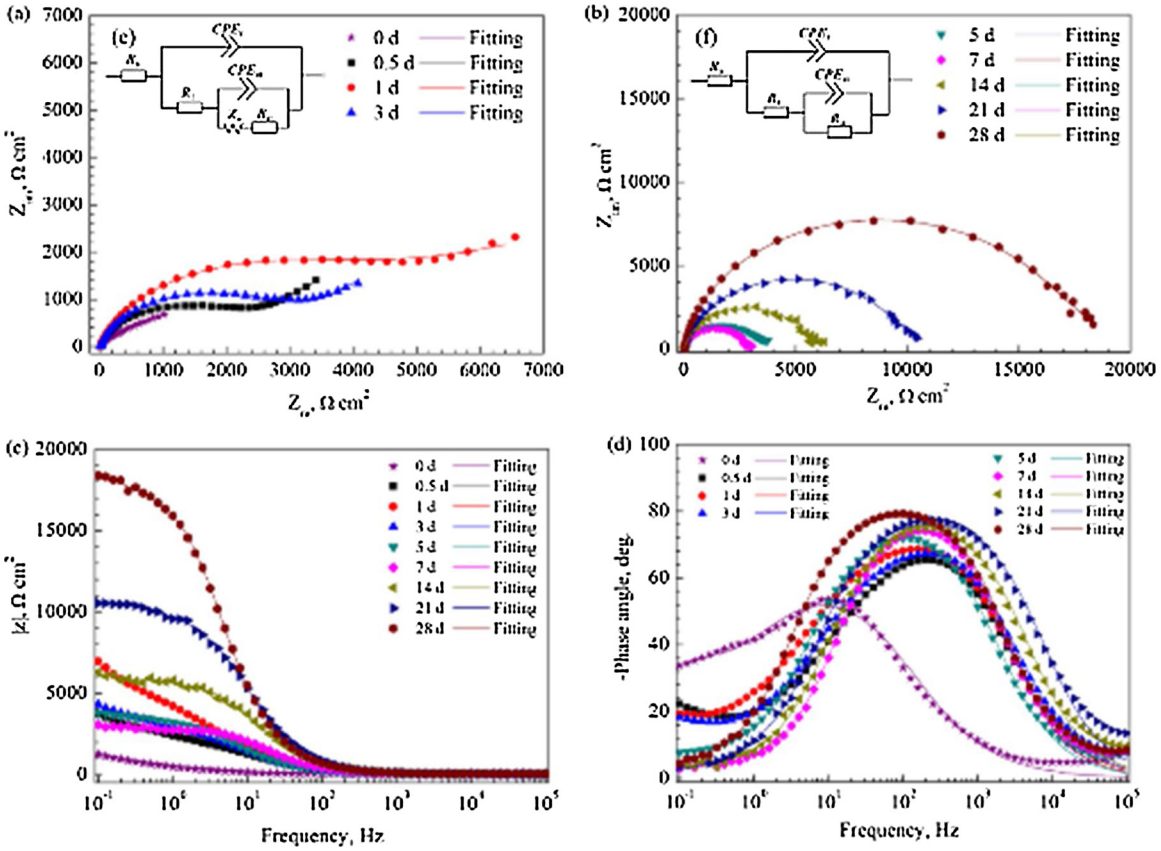

Fig. 14. EIS and the fitted results of pure Zn immersed for different time: (a, b) Nyquist plots, (c) Bode plots of |Z| vs. frequency, (d) Bode plots of phase angle vs. frequency in the artificial plasma; equivalent circuits (inserted in Fig. a and b) for the samples after immersion for different time: (e) 0.5 d, 1 d and 3 d, (f) 0 d, 5 d, 7 d, 14 d, 21 d and 28 d.

Table 6
Fitting parameters of pure Zn immersed in AP for different times.

Immersion time	CPE_f (10^{-5} Ω^{-1} cm^{-2} s^{n1})	n_1	R_f (kΩ cm^2)	CPE_{dl} (10^{-4} Ω^{-1} cm^{-2} s^{n2})	n_2	R_{ct} (kΩ cm^2)	W (10^{-4} Ω^{-1} cm^{-2} s$^{0.5}$)	χ^2 (10^{-3})
0 d	39.92 ± 5.17	0.70 ± 0.02	0.31 ± 0.10	1.31 ± 0.18	0.89 ± 0.06	0.94 ± 0.12		2.58 ± 0.32
0.5 d	1.73 ± 0.41	0.84 ± 0.02	2.76 ± 0.16	0.72 ± 0.08	0.75 ± 0.01	1.71 ± 0.18	8.09 ± 2.44	0.68 ± 0.10
1 d	1.23 ± 0.16	0.86 ± 0.01	4.45 ± 0.32	0.88 ± 0.05	0.51 ± 0.01	3.38 ± 1.79	3.24 ± 1.00	0.87 ± 0.10
3 d	1.37 ± 0.22	0.86 ± 0.01	2.45 ± 0.18	3.88 ± 1.51	0.54 ± 0.13	2.10 ± 0.67	7.19 ± 4.76	0.64 ± 0.05
5 d	1.46 ± 0.14	0.87 ± 0.01	3.01 ± 0.21	8.76 ± 4.28	0.59 ± 0.04	0.88 ± 0.37		0.94 ± 0.09
7 d	0.67 ± 0.02	0.91 ± 0.01	2.17 ± 0.53	2.66 ± 0.61	0.98 ± 0.01	0.42 ± 0.14		1.72 ± 0.41
14 d	0.25 ± 0.17	0.92 ± 0.02	5.23 ± 0.39	0.39 ± 0.12	0.90 ± 0.02	1.20 ± 0.36		1.15 ± 0.71
21 d	0.35 ± 0.05	0.90 ± 0.01	9.79 ± 0.16	2.77 ± 1.01	0.90 ± 0.06	1.69 ± 1.63		1.65 ± 0.88
28 d	0.35 ± 0.04	0.92 ± 0.01	21.22 ± 3.42	3.71 ± 2.29	0.88 ± 0.10	3.70 ± 1.92		2.15 ± 0.32

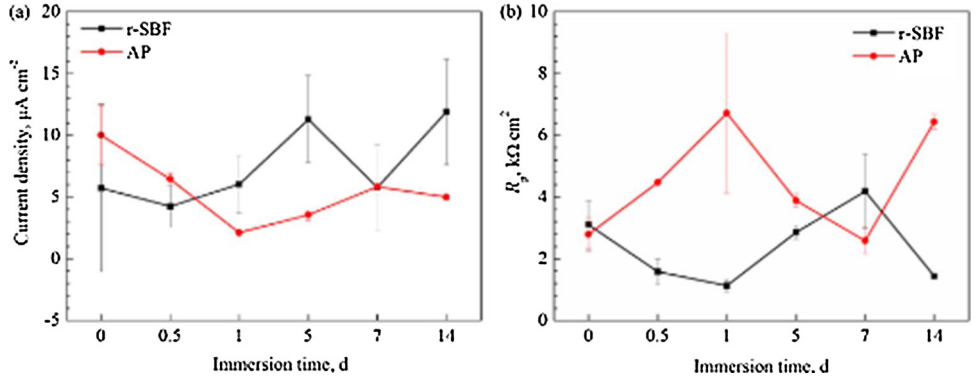

Fig. 15. Comparative electrochemical parameters of pure Zn tested in r-SBF and AP: (a) current density i_{corr} obtained from PDP curves and (b) polarization resistance R_p obtained from EIS measurements.

Table 7
Corrosion rate along with related parameters of pure Zn obtained from weight loss, EIS, LPR data.

Immersion time	Weight loss		LPR			EIS		
	W (mg cm^2)	CR_w (μm y^{-1})	R_{LPR} (kΩ cm^2)	i_{corr} (μA cm^{-2})	CR_i (μm y^{-1})	$R_{p\text{-}EIS}$ (kΩ cm^2)	$i_{corr\text{-}EIS}$ (μA cm^{-2})	CR_{EIS} (μm y^{-1})
0 d	–	–	2.31 ± 0.24	10.53 ± 1.57	156.87 ± 23.46	2.79 ± 0.54	8.84 ± 1.76	132.70 ± 37.78
0.5 d	0.04 ± 0.04	13.31 ± 11.5	4.97 ± 0.43	6.46 ± 0.48	96.23 ± 7.08	4.50 ± 0.05	7.10 ± 0.19	105.81 ± 2.82
1 d	0.04 ± 0.04	6.65 ± 5.76	5.54 ± 0.77	2.12 ± 0.30	31.55 ± 4.48	7.50 ± 1.77	1.59 ± 0.32	23.76 ± 4.70
3 d	0.52 ± 0.07	38.83 ± 5.08	4.44 ± 0.35	3.42 ± 0.62	50.97 ± 9.25	4.32 ± 0.86	3.61 ± 0.10	53.86 ± 14.86
5 d	0.58 ± 0.08	25.96 ± 3.46	5.90 ± 0.47	3.62 ± 0.33	53.93 ± 4.90	3.89 ± 0.21	5.48 ± 0.36	81.63 ± 5.35
7 d	1.21 ± 0.26	38.99 ± 8.36	2.46 ± 0.51	5.83 ± 0.63	86.84 ± 9.30	2.59 ± 0.44	5.50 ± 0.42	82.02 ± 6.34
14 d	1.62 ± 0.05	26.15 ± 0.82	3.01 ± 0.08	4.99 ± 0.23	74.45 ± 3.40	6.43 ± 0.24	2.33 ± 0.13	34.82 ± 1.96
21 d	1.80 ± 0.07	19.34 ± 0.73	17.77 ± 7.27	1.04 ± 0.35	15.56 ± 5.26	11.49 ± 1.79	1.51 ± 0.38	22.48 ± 5.64
28 d	2.05 ± 0.02	16.52 ± 0.21	26.38 ± 4.55	0.76 ± 0.18	11.31 ± 2.79	24.92 ± 5.27	1.04 ± 0.63	12.40 ± 4.98

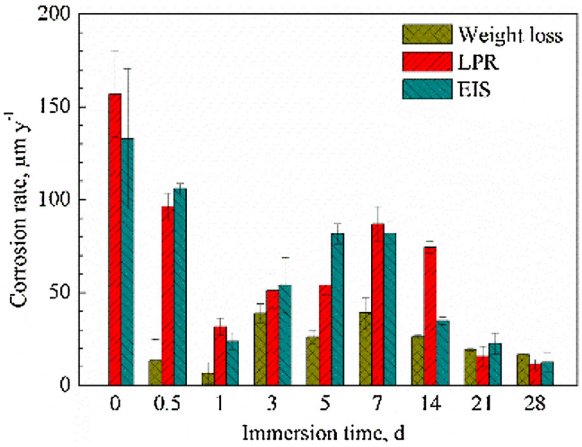

Fig. 16. Corrosion rates calculated from weight loss, LPR and EIS methods at different immersion time.

It has been accepted that the interactions between albumin and metal surfaces include both adsorption and chelation process [63]. Under the neutral physiological conditions, BSA molecules are negatively charged (isoelectric pH 4.7–4.9) [64]. Divalent Zn^{2+} ions can be combined to C═O and C—N groups by electrostatic interactions as detected by FTIR. In the first day of immersion (Fig. 18a), the Zn^{2+} ions near the surface serve as bridging agents to enhance the gradual adsorption of BSA (Fig. 3a and b). The adsorbed BSA protects the samples from corrosion to some extent, leading to a decrease of corrosion rate (Fig. 16). In this stage, desorption of BSA molecules proceeds at the same time, which accounts for the appearance of Warburg impendence in the Nyquist plots (Fig. 14a).

As shown in Fig. 10a, the release Zn^{2+} amount shows an obvious uptrend during the immersion of 3–7 d. And in the same immersion period, the electrochemical tests reveal an increased current density and decreased impendence. These results reflect that the effect of chelation of BSA with Zn^{2+} surpasses BSA adsorption, leading to the evident dissolution of metal matrix (Fig. 18b). Thus the corrosion rates are increased in the second stage. According to the previous study [65], Zn^{2+} can form pentacoordinate Zn (II) binding geometry through MBS/Site A in BSA, with the apical position taken up by water or an anion (e.g. Cl^-). The UV–vis spectra are used detect the complex of Zn^{2+} and BSA in the solution. As shown in Fig. 17, the absorption peak for BSA is detected around 280 nm. The fresh solution is used as control. The solution placed after one day without soaking the sample shows the similar spectrum as the fresh solution (Fig.17a), which excludes the

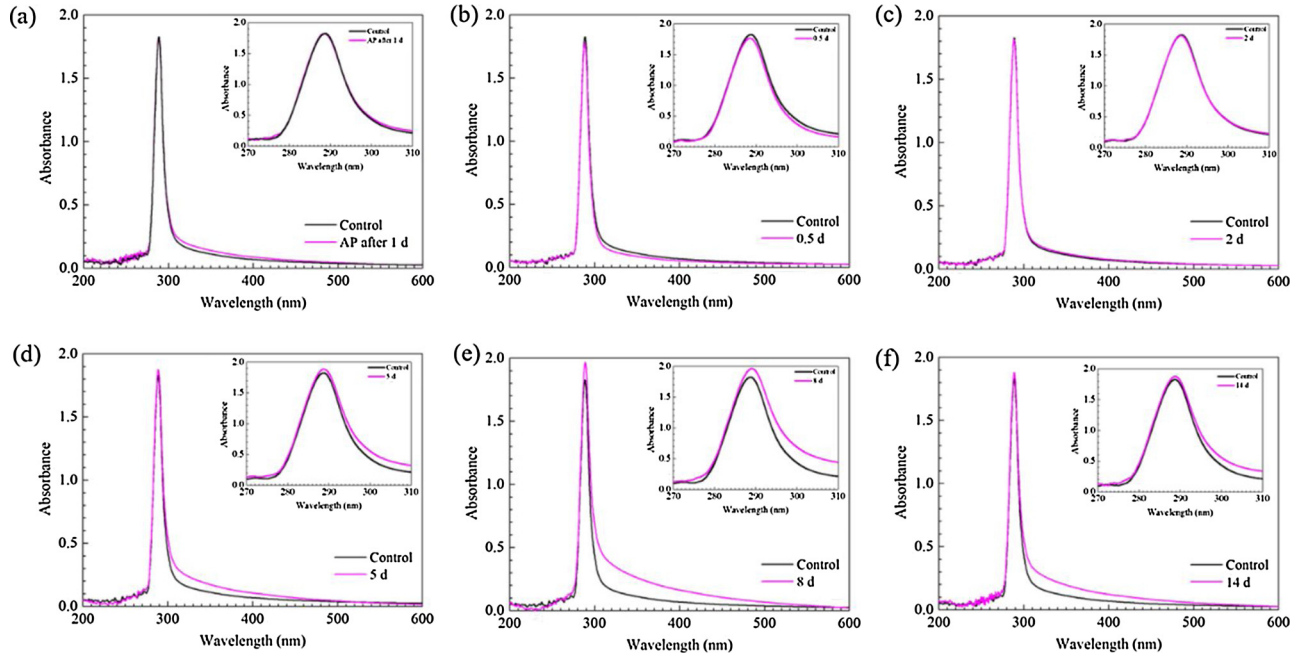

Fig. 17. UV–vis spectra of the AP solution after different immersion time: (a) AP solution after one day without soaking the sample; (b) 0.5 d, (c) 3 d, (d) 5 d, (e) 8 d and (f) 14 d. Control: the fresh solution.

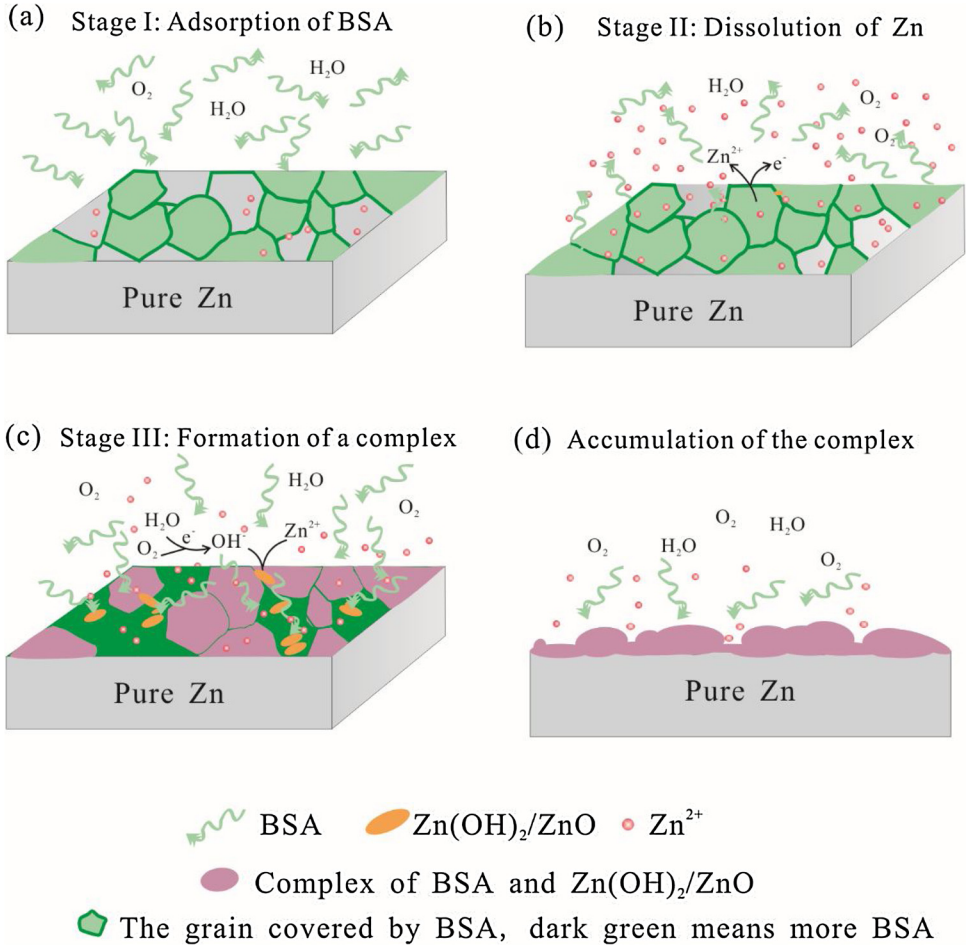

Fig. 18. Schematic illustration of corrosion process of the pure Zn immersed in artificial plasma: (a) adsorption of BSA at initial immersion stage; (b) dissolution of pure Zn; (c) formation of a complex of BSA and Zn(OH)/ZnO; (d) accumulation of the complex on sample surface.

changes of BSA itself in the solution. In the first 2 days (Fig. 17b and c), no obvious change is observed in the peak intensity or position. After longer immersion, the absorption peak intensity is gradually increased, which is followed by the shift in the maximum wavelength, indicating the disorder of the BSA structure. Combined with Fig. 10 a, the released amount of Zn^{2+} is higher during the immersion between 5–14 days, which may account for the obvious change of UV–vis spectra for 5 d, 8 d and 14 d (Fig. 17d–f).

During the immersion, the released Zn^{2+} ions promote formation of zinc oxide/hydroxide on pure Zn surfaces. As reported by Bhunia et al [66] the binding constant K along with the number of binding sites (n) between BSA and ZnO nanorods are 1.84×10^3 M^{-1} and 1.11, respectively, which indicate that a positive cooperation takes place. As shown in FTIR spectra, no peak shift is observed during the immersion for 28 d, which suggests that combination bonds of BSA molecules and Zn substrate remain unchanged. According to Zhang et al [67], BSA was firstly connected to Zn^{2+} via electrostatic interactions. The adsorbed Zn^{2+} provide the nuclei for the growth of ZnO by hydrolysis, forming the BSA/ZnO complex. However, S. Chakraborti et al [68] pointed that the interaction of ZnO and BSA relied on both electrostatic and hydrophobic forces, only that the exact location of ZnO within BSA was not ascertained. Thus, a complex of BSA and ZnO/$Zn(OH)_2$ forms on the pure Zn surface during the immersion (Fig. 18c). With the extension of immersion time, especially after 7 d (in the third stage) the complex accumulates on sample surfaces (Fig. 18d), leading to the gradual disappear of grain boundary as shown in the AFM images (Fig. 4e–h). Meanwhile, the complex, which in turn, act as a physical barrier for electrons, anions and cations transport. Therefore, the substrates are protected from the corrosive medium and the corrosion resistance of pure Zn is improved after immersion for longer time (Fig. 16).

5. Conclusion

In this study, the influences of BSA on corrosion process of pure Zn in artificial plasma were characterized by immersion test and electrochemical test. The results were summarized as follows:

(1) Overall, in the presence of BSA, pure Zn undergoes uniform corrosion during the immersion for 28 d.
(2) The corrosion products are mainly comprised of BSA and ZnO/Zn$(OH)_2$.
(3) Three stages of the corrosion process of pure Zn can be distinguished in the presence of BSA: in the first day, BSA adsorption protects the substrate from dissolution; but the chelation of BSA and Zn^{2+} increase the corrosion rate during 3–7 d immersion; after 7 d the corrosion resistance of pure Zn is improved by the complex accumulation on sample surfaces.
(4) The corrosion rates estimated by the weight loss, LPR and EIS are 16.52 ± 0.21, 11.31 ± 2.79, 12.44 ± 5.37 μm y^{-1}, respectively. These values are close to the design criteria for stent materials.
(5) The influences of protein on biomedical materials should be taken into consideration in the in vitro tests.

Data availability

All research data supporting this publication are directly available

within this publication.

Acknowledgements

Authors are grateful for the National Key Research and Development Program2016YFC251100, National Natural Science Foundation of China (Grant No. 51503014 and No. 51501008) and financial support from the State Key Laboratory for Advanced Metals and Materials (No. 2016Z-03). L.W. thanks Drs. Chaofang Dong and Yu Yan for their valuable discussion.

References

[1] J. Kubásek, D. Vojtěch, Zn-based Alloys As an Alternative Biodegradable Materials, Metal 2012, Brno, Czech Republic, 2012 25 May 2012.
[2] P.K. Bowen, J. Drelich, J. Goldman, Zinc exhibits ideal physiological corrosion behavior for bioabsorbable stents, Adv. Mater. 25 (2013) 2577–2582.
[3] Y.F. Zheng, X.N. Gu, F. Witte, Biodegradable metals, Mater. Sci. Eng. R 77 (2014) 1–34.
[4] P. Sotoudeh Bagha, S. Khaleghpanah, S. Sheibani, M. Khakbiz, A. Zakeri, Characterization of nanostructured biodegradable Zn-Mn alloy synthesized by mechanical alloying, J. Alloys. Compd. 735 (2018) 1319–1327.
[5] Z.Z. Shi, J. Yu, X.F. Liu, L.N. Wang, Fabrication and characterization of novel biodegradable Zn-Mn-Cu alloys, J. Mater. Sci. Technol. Res. 34 (2018) 1008–1015.
[6] Z.Z. Shi, J. Yu, X.F. Liu, Microalloyed Zn-Mn alloys: from extremely brittle to extraordinarily ductile at room temperature, Mater. Design 144 (2018) 343–352.
[7] C. Wang, H.T. Yang, X. Li, Y.F. Zheng, *In vitro* evaluation of the feasibility of commercial Zn alloys as biodegradable metals, J. Mater. Sci. Technol. Res. 32 (2016) 909–918.
[8] P.K. Bowen, E.R. Shearier, S. Zhao, R.J. Guillory, F. Zhao, J. Goldman, J.W. Drelich, Biodegradable metals for cardiovascular stents: from clinical concerns to recent Zn-alloys, Adv. Healthcare Mater. 5 (2016) 1121–1140.
[9] N.S. Murni, M.S. Dambatta, S.K. Yeap, G.R. Froemming, H. Hermawan, Cytotoxicity evaluation of biodegradable Zn-3Mg alloy toward normal human osteoblast cells, Mater. Sci. Eng. C 49 (2015) 560–566.
[10] C.J. Frederickson, J.Y. Koh, A.I. Bush, The neurobiology of zinc in health and disease, Mat. Rev. Neurosci. 6 (2005) 449–462.
[11] H.F. Li, X.H. Xie, Y.F. Zheng, Y. Cong, F.Y. Zhou, K.J. Qiu, X. Wang, S.H. Chen, L. Huang, L. Tian, Development of biodegradable Zn-1X binary alloys with nutrient alloying elements Mg, Ca and Sr, Sci. Rep. 5 (2015) 10719–10733.
[12] J.H. Weiss, S.L. Sensi, J.Y. Koh, Zn(II): a novel ionic mediator of neural injury in brain disease, Trends Pharmacol. Sci. 21 (2000) 395–401.
[13] B. Hennig, M. Toborek, C.J. Mcclain, Antiatherogenic properties of zinc: implications in endothelial cell metabolism, Nutrition 12 (1996) 711–717.
[14] T.A. Ostomel, Q. Shi, P.K.S. And, G.D. Stucky, Metal oxide surface charge mediated hemostasis, Langmuir 23 (2012) 11233–11238.
[15] H. Yang, C. Wang, C. Liu, H. Chen, Y. Wu, J. Han, Z. Jia, W. Lin, D. Zhang, W. Li, W. Yuan, H. Guo, H. Li, G. Yang, D. Kong, D. Zhu, K. Takashima, L. Ruan, J. Nie, X. Li, Y. Zheng, Evolution of the degradation mechanism of pure zinc stent in the one-year study of rabbit abdominal aorta model, Biomaterials 145 (2017) 92–105.
[16] J. Cheng, B. Liu, Y.H. Wu, Y.F. Zheng, Comparative *in vitro* study on pure metals (Fe, Mn, Mg, Zn and W) as biodegradable metals, J. Mater. Sci. Technol. Res. 29 (2013) 619–627.
[17] Y.Q. Chen, W.T. Zhang, M.F. Maitz, M.Y. Chen, H. Zhang, J.L. Mao, Y.C. Zhao, N. Huang, G.J. Wan, Comparative corrosion behavior of Zn with Fe and Mg in the course of immersion degradation in phosphate buffered saline, Corros. Sci. 111 (2016) 541–555.
[18] H.F. Li, H.T. Yang, Y.F. Zheng, F.Y. Zhou, K.J. Qiu, X. Wang, Design and characterizations of novel biodegradable ternary Zn-based alloys with IIA nutrient alloying elements Mg, Ca and Sr, Mater. Design 83 (2015) 95–102.
[19] E. Mostaed, M. Sikorajasinska, A. Mostaed, S. Loffredo, A.G. Demir, B. Previtali, D. Mantovani, R. Beanland, M. Vedani, Novel Zn-based alloys for biodegradable stent applications: design, development and in vitro degradation, J. Mech. Behav. Biomed. Mater. 60 (2016) 581–602.
[20] K.B. Törne, M. Larsson, A. Norlin, J. Weissenrieder, Degradation of zinc in saline solutions, plasma, and whole blood, J. Biomed. Mater. Res. B 104 (2015) 1141–1151.
[21] K.B. Törne, A. Örnberg, J. Weissenrieder, Characterization of the protective layer formed on zinc in whole blood, Electrochim. Acta 258 (2017) 1476–1483.
[22] A. Yamamoto, S. Hiromoto, Effect of inorganic salts, amino acids and proteins on the degradation of pure magnesium in vitro, Mat. Sci. Eng. C 29 (2009) 1559–1568.
[23] S. Karimi, T. Nickchi, A. Alfantazi, Effects of bovine serum albumin on the corrosion behaviour of AISI 316L, Co-28Cr-6Mo, and Ti-6Al-4V alloys in phosphate buffered saline solutions, Corros. Sci. 53 (2011) 3262–3272.
[24] N.T. Kirkland, J. Lespagnol, N. Birbilis, M.P. Staiger, A survey of bio-corrosion rates of magnesium alloys, Corros. Sci. 52 (2010) 287–291.
[25] C.L. Liu, Y.J. Wang, R.C. Zeng, X.M. Zhang, W.J. Huang, P.K. Chu, In vitro corrosion degradation behaviour of Mg-Ca alloy in the presence of albumin, Corros. Sci. 52 (2010) 3341–3347.
[26] J. Walker, S. Shadanbaz, N.T. Kirkland, E. Stace, T. Woodfield, M.P. Staiger, G.J. Dias, Magnesium alloys: predicting in vivo corrosion with in vitro immersion testing, J. Biomed. Mater. Res. B 100B (2012) 1134–1141.
[27] J. Zhang, N. Kong, Y. Shi, J. Niu, L. Mao, H. Li, M. Xiong, G. Yuan, Influence of proteins and cells on in vitro corrosion of Mg-Nd-Zn-Zr alloy, Corros. Sci. 85 (2014) 477–481.
[28] Y. Wang, S.L. Chu, V.L. Chao, S.Y. Ming, E.K. Teo, L.N. Moh, In vitro degradation behavior of M1A magnesium alloy in protein-containing simulated body fluid, Mater. Sci. Eng. C 31 (2011) 579–587.
[29] G.C.F. Clark, D.F. Williams, The effects of proteins on metallic corrosion, J. Biomed. Mater. Res. A 16 (1982) 125–134.
[30] Y.C. Tang, S. Katsuma, S. Fujimoto, S. Hiromoto, Electrochemical study of Type 304 and 316L stainless steels in simulated body fluids and cell cultures, Acta Biomater. 2 (2006) 709–715.
[31] G.T. Burstein, C. Liu, Nucleation of corrosion pits in Ringer's solution containing bovine serum, Corros. Sci. 49 (2007) 4296–4306.
[32] F. Contu, B. Elsener, H. Böhni, Corrosion behaviour of CoCrMo implant alloy during fretting in bovine serum, Corros. Sci. 47 (2005) 1863–1875.
[33] ISO 10993-15, Biological Evaluation of Medical Devices- Part 15: Identification and Quantification of Degradation Products From Metals and Alloys, 1st ed., (2000), p. 2000.
[34] ASTM Standard 31-73, Standard Practice for Laboratory Immersion Corrosion Testing of Metals, Reapproved, (2004).
[35] ISO 8407, Corrosion of Metals and Alloys-removal of Corrosion Products from Corrosion Test Specimens, 2nd ed., (2009), p. 2009.
[36] Z. Gui, Z. Kang, Y. Li, Mechanical and corrosion properties of Mg-Gd-Zn-Zr-Mn biodegradable alloy by hot extrusion, J. Alloys. Compd. 685 (2016) 222–230.
[37] Y. Yu, H. Yang, Y. Su, L. Qiao, Albumin adsorption on CoCrMo alloy surfaces, Sci. Rep. 5 (2015) 18403–18413.
[38] J.Y. Yu, Y.J. Kong, Y. Zhang, J. zhang, X.Y. Yang, G.F. Zhang, Z.G. Su, M.L. Wang, Effects of hydrophobicity and content of ligands on silica surface on adsorption behavior of proteins, Chin. J. Process. Eng. 16 (2016) 774–780.
[39] H. Qing, Y. He, F. Sheng, Z. Tao, Effects of pH and metal ions on the conformation of bovine serum albumin in aqueous solution: an attenuated total reflection (ATR) FTIR spectroscopic study, Spectrochim. Acta A 52 (1996) 1795–1800.
[40] A.E. Ledesma, D.M. Chemes, Mdl.A. Frías, Md.P. Guauque Torres, Spectroscopic characterization and docking studies of ZnO nanoparticle modified with BSA, Appl. Surf. Sci. 412 (2017) 177–188.
[41] C. Guo, X. Guo, W. Chu, N. Jiang, H. Li, Spectroscopic study of conformation changes of bovine serum albumin in aqueous environment, Chin. Chem. Lett. (2019), https://doi.org/10.1016/j.cclet.2019.02.023.
[42] Y. Li, Y.F. Sun, C.B. Zhao, Z.L. Tan, B.K. Qi, Analysis of Raman spectroscopy and fluorescence spectroscopy for soy protein isolate during vitro simulated digestion process, J. Chin. Inst. Food Sci. Technol. 1 (2019) 1–8.
[43] K. Vijayarangamuthu, S. Rath, One-step synthesis of Au-coated porous silicon as a surface enhanced Raman scattering substrate for biomolecule detection, Mater. Lett. 204 (2017) 115–119.
[44] L. De Plano, E. Fazio, M.G. Rizzo, D. Franco, S. Carnazza, S. Trusso, F. Neri, S. Guglielmino, Phage-based assay for rapid detection of bacterial pathogens in blood by Raman spectroscopy, J. Immunol. Methods 465 (2019) 45–52.
[45] H.H. Lee, M. Bae, S.H. Jo, J.K. Shin, H.S. Dong, C.H. Won, J.H. Lee, Differential-mode HEMT-based biosensor for real-time and label-free detection of C-reactive protein, Sens. Actuators B Chem. 234 (2016) 316–323.
[46] B.E.T. Bautista, M.L. Carvalho, A. Seyeux, S. Zanna, P. Cristiani, B. Tribollet, P. Marcus, I. Frateur, Effect of protein adsorption on the corrosion behavior of 70Cu-30Ni alloy in artificial seawater, Bioelectrochemistry 97 (2014) 34–42.
[47] P. Wan, X. Lin, L.L. Tan, L. Li, W.R. Li, K. Yang, Influence of albumin and inorganic ions on electrochemical corrosion behavior of plasma electrolytic oxidation coated magnesium for surgical implants, Appl. Surf. Sci. 282 (2013) 186–194.
[48] E. Vanea, V. Simon, XPS study of protein adsorption onto nanocrystalline aluminosilicate microparticles, Appl. Surf. Sci. 257 (2011) 2346–2352.
[49] L.Y. Yang, L.L. Xin, W. Gu, J.L. Tian, S.Y. Liao, P.Y. Du, Y.Z. Tong, Y.P. Zhang, R. Lv, J.Y. Wang, X. Liu, A new carboxyl-copper-organic framework and its excellent selective absorbability for proteins, J. Solid State Chem. 218 (2014) 64–70.
[50] O. Olivares, N.V. Likhanova, B. Gómez, J. Navarrete, M.E. Llanos-Serrano, E. Arce, J.M. Hallen, Electrochemical and XPS studies of decylamides of α-amino acids adsorption on carbon steel in acidic environment, Appl. Surf. Sci. 252 (2006) 2894–2909.
[51] W. Wang, F. Mohammadi, A. Alfantazi, Corrosion behaviour of niobium in phosphate buffered saline solutions with different concentrations of bovine serum albumin, Corros. Sci. 57 (2012) 11–21.
[52] B. Lindberg, A. Berndtsson, R. Nilsson, R. Nyholm, O. Exner, An esca investigation of ambident ions and tautomerism. N-cyanobenzamides and benzohydroxamic acids, Chem. Inform. 9 (1978) 353–359.
[53] E. Salehi, R. Naderi, B. Ramezanzadeh, Synthesis and characterization of an effective organic/inorganic hybrid green corrosion inhibitive complex based on zinc acetate/Urtica Dioica, Appl. Surf. Sci. 396 (2017) 1499–1514.
[54] Y. Song, E.H. Han, D. Shan, D.Y. Chang, B.S. You, The effect of Zn concentration on the corrosion behavior of Mg-x Zn alloys, Corros. Sci. 65 (2012) 322–330.
[55] C.M. Wang, J. Shen, F.X. Xie, B. Duan, X. Xie, A versatile dopamine-induced intermediate layer for polyether imides (PEI) deposition on magnesium to render robust and high inhibition performance, Corros. Sci. 122 (2017) 32–40.
[56] A.D. King, N. Birbilis, J.R. Scully, Accurate electrochemical measurement of magnesium corrosion rates; a combined impedance, mass-loss and hydrogen collection study, Electrochim. Acta 121 (2014) 394–406.
[57] M. Mouanga, P. Berçot, J.Y. Rauch, Comparison of corrosion behaviour of zinc in NaCl and in NaOH solutions. Part I: corrosion layer characterization, Corros. Sci. 52 (2010) 3984–3992.
[58] L.J. Liu, Y. Meng, C.F. Dong, Y. Yan, A.A. Volinsky, L.N. Wang, Initial formation of

corrosion products on pure zinc in simulated body fluid, J. Mater. Sci. Technol. 32 (2018) 2271–2282.
[59] F. Seuss, S. Seuss, M.C. Turhan, B. Fabry, S. Virtanen, Corrosion of Mg alloy AZ91D in the presence of living cells, J. Biomed. Mater. Res. B. 99 (2011) 276–281.
[60] R.C. Zeng, X.T. Li, S.Q. Li, F. Zhang, E.H. Han, In vitro degradation of pure Mg in response to glucose, Sci. Rep. 5 (2015) 13026–13040.
[61] P.K. Bowen, E.R. Shearier, S. Zhao, F. Zhao, J. Goldman, J.W. Drelich, Biodegradable metals for cardiovascular stents: from clinical concerns to recent Zn-alloys, Adv. Healthcare. Mater. 5 (2016) 1121–1140.
[62] J. Yang, C.D. Yim, B.S. You, Effects of solute Zn on corrosion film of Mg-Sn-Zn alloy formed in NaCl solution, J. Electrochem. Soc. 163 (2016) C839–C844.
[63] S.E. Harandi, P.C. Banerjee, C.D. Easton, R.R. Singh, Influence of bovine serum albumin in Hanks' solution on the corrosion and stress corrosion cracking of a magnesium alloy, Mater. Sci. Eng. C 80 (2017) 335–345.
[64] F. El-Taib Heakal, A.M. Bakry, Serum albumin can influence magnesium alloy degradation in simulated blood plasma for cardiovascular stenting, Mater. Chem. Phys. 220 (2018) 35–49.
[65] W. Bal, M. Sokolowska, E. Kurowska, P. Faller, Binding of transition metal ions to albumin: sites, affinites and rates, BBA-Biomembranes 1830 (2013) 5444–5455.
[66] A.K. Bhunia, T. Kamilya, S. Saha, Synthesis, Characterization of ZnO nanorods and its interaction with albumin protein, Mater. Today Proc. 3 (2016) 592–597.
[67] T. Zhang, Y.M. Zhou, Y.J. Wang, L.P. Zhang, H.Y. Wang, X. Wu, Fabrication of hierarchical nanostructured BSA/ZnO hybrid nanoflowers by a self-assembly process, Mater. Lett. 128 (2014) 227–230.
[68] C. Soumyananda, J. Prachi, C. Devlina, S. Virendra, Z.A. Ansari, S.P. Singh, C. Pinak, Interaction of polyethyleneimine-functionalized ZnO nanoparticles with bovine serum albumin, Langmuir 28 (2012) 11142–11152.